crystals

MDPI

Article

The Textural Motif of Foliated Calcite in Ostreoidea (Mollusca)

Erika Griesshaber [1], Anna Sancho Vaquer [1,*], Antonio G. Checa [2], Carmen Salas [3], Elizabeth M. Harper [4] and Wolfgang W. Schmahl [1]

[1] Department of Geo- and Environmental Sciences, Ludwig-Maximilians-Universität München, 80333 Munich, Germany
[2] Departamento de Estratigrafía y Paleontología, Universidad de Granada, 18071 Granada, Spain
[3] Departamento de Biología Animal, Facultad de Ciencias, Universidad de Málaga, 29071 Málaga, Spain
[4] Department of Earth Sciences, University of Cambridge, Cambridge CB2 3EQ, UK
* Correspondence: a.sancho@campus.lmu.de

Abstract: The microstructure of bivalve foliated calcite is extraordinary. It consists of units formed of stacks of folia with individual folia consisting of arrowhead-ended crystal laths. We investigated the texture of the foliated microstructure, the texture of individual and arrays of folia and the texture of assemblies of foliated units of the gryphaeid oyster *Hyotissa hyotis* with low kV, high-resolution, electron backscatter diffraction (EBSD). We base our understanding of the foliated texture on the combined interpretation of crystallographic aspects of individual and stacks of folia with the nature of crystal organization in a folium, a foliated unit and in foliated unit aggregations. Calcite c- and a*-axes arrangement in a folium is single-crystal-like. Due to the parallel organization of adjacent laths in a folium and the stacked arrangement of folia in a foliated unit, the assembly of calcite c- and a*-axes in foliated units is graded. The result is a ring-like distribution of c- and a*-axes orientations in the pole figures; nonetheless, the orientation rings are substructured by c- and a*-axes orientation clusters. The direction of the arrowhead endings of the laths is coincident with the growth direction of the shell. The morphology of arrowheaded laths initiates the formation of planes with {105}, {106} directions and a parallel orientation to the inner shell surface. *H. hyotis*'s foliated microstructure has a specific texture that is not fully understood. We discuss axial, spherulitic, turbostratic-like textures the foliated microstructure and suggest that the foliated texture of *H. hyotis* can, to some degree, be described with a turbostratic pattern.

Keywords: turbostratic texture; high-resolution EBSD; assembly of folia and foliated units; graded c- and a*-axes orientations of biocalcite; spherulitic texture of biocalcite; axial texture of biocalcite

Academic Editor: Alessandra Toncelli

Received: 31 January 2025
Revised: 19 February 2025
Accepted: 28 February 2025
Published: 4 March 2025

Citation: Griesshaber, E.; Sancho Vaquer, A.; Checa, A.G.; Salas, C.; Harper, E.M.; Schmahl, W.W. The Textural Motif of Foliated Calcite in Ostreoidea (Mollusca). *Crystals* **2025**, *15*, 244. https://doi.org/10.3390/cryst15030244

1. Introduction

Ostreoidea shells are composites of calcium carbonate and biopolymers. Apart from myostracal and hinge aragonite, the Ostreoidea secrete low-Mg calcite [1] for shell generation. Shell formation starts between the outer and the middle mantle folds, within the periostracal groove [2]. The peripostacum reflects back at the shell margin and mineralization and shell deposition start below it [2,3].

Ostreoidea form their shells with a large variety of Ca-carbonate microstructures, summarized by Sancho Vaquer et al. [4]. The largest part of the Ostreoidea shell consists of foliated calcite [2,5–12], complemented, along the external surface of both valves, with a layer of columnar prismatic calcite [12–15] and, along sections of the external surface of the lower valve, with a cementation layer comprising granular calcite [16–19]. The muscle attachment sites, the myostraca, are formed of prismatic aragonite. The columnar prismatic, foliated, granular calcite and prismatic aragonite microstructures generate compact shell layers. The Ostreoidea superfamily includes the Ostreidae and the Gryphaeidae families, and both incorporate large volumes of cavities and voids into their shells. Ostreidae include a meshwork of calcite blades, generating the chalk lenses [2,10,20–24]. Gryphaeidae incorporate into the shell arrays of submicrometer- to micrometer-sized holes, the vesicles [4,25–27]. Foliated calcite forms the bulk of the Ostreoidea shell, and all other shell microstructures, the columnar prismatic, chalky, vesicular and granular crystal assemblies, are in topological relation to the arrangement of the foliated crystals [4]. The foliated microstructure of Ostreoidea shells has often been investigated, mainly with light microscopy, SEM imaging, X-ray diffraction (XRD) [12,17–19,22,25] and, to some degree, conventional electron backscatter diffraction (EBSD) [13,22].

The Ostreoidea foliated microstructure is very intricate, and its crystal organization is very specific. Even though it has been investigated with XRD [6,11,28,29] and conventional EBSD [22], the texture pattern of Ostreoidea foliated calcite is not fully deciphered and understood yet. Laboratory-based XRD measurements average over comparatively large sections of the shell and give no microstructure-related information. Depending on the material in question, the minimal step size of conventional EBSD is, in general, above 0.5 µm. Hence it is too coarse for the mapping of the very fine-scaled arrangement of folia in the foliated shell. In this study, we concentrate on the nature of the Ostreoidea foliated calcite texture, rooted in the Ostreoidea foliated microstructure, and describe its small-scale structural–crystallographic aspects. An in-depth crystallographic study of the Ostreoidea foliated calcite texture will be given by Schmahl et al. [30]. We chose to investigate the texture of the foliated microstructure of the gryphaeid species *Hyotissa hyotis* (Linnaeus, 1758). This oyster forms large and thick shells, has a circum-tropical distribution and lives within the upper 50 m of the water column [31–37]. Apart from myostracal aragonite, *H. hyotis* forms its shell of calcite.

In our study, we describe and discuss the nature of the foliated calcite texture of *H. hyotis* and base the understanding of the latter on the inter-relation between specific characteristics of the foliated microstructure, e.g., the misorientation between crystals, and the different modes of foliated calcite crystal orientations. This is performed through small-scale crystallographic results of *H. hyotis*'s foliated crystals obtained from low kV, high-resolution EBSD measurements. We demonstrate the gradedness of the c- and a*-axes orientation of a stack of folia for *H. hyotis* and discuss the crystallographic differences and similarities between turbostratic, spherulitic and axial calcite texture patterns which may be invoked to describe the nature of the *H. hyotis* foliated texture pattern.

2. Materials and Methods

2.1. Materials

We investigated the shell of the gryphaeid oyster *Hyotissa hyotis*. The specimens were sampled at Guadeloupe in the Caribbean Sea.

2.2. Methods

The valves were cut transversely. Entire shell segments were embedded into epoxy. Sample surfaces were treated with eight mechanical grinding and polishing steps to obtain a highly polished surface. The final polishing step consisted of etch polishing with colloidal alumina performed with a vibratory polisher. EBSD measurements required 4–6 nm carbon coating; for FE-SEM imaging, the samples were coated with 5 nm Pt/Pd.

EBSD measurements were performed with a Hitachi (Tokyo, Japan) SU5000 field emission SEM, equipped with an Oxford Instruments (Abingdon, UK) Nordlys II EBSD detector. The SEM operation in EBSD measurements was mainly at 12 and 15 kV, and for a few measurements, at 8 kV. For EBSD data evaluation, the Oxford Instruments (Abingdon, UK) HKL CHANNEL 5 and AZTec Crystal software were used. Most measurements were performed with increments of 100 to 200 nm, and none of the measurements had a step size higher than 350 nm. This is a necessary requirement for the crystallographic investigation of the foliated shell, as the foliated calcite of the Ostreoidea consists of parallel arrays of 200 to 400 nm thick, 2–4 µm wide and up to 20 µm long folia (e.g., this study and [6,11,22]). Thus, for an in-depth understanding of the foliated microstructure and the foliated texture, it is essential to perform the EBSD scans with very small step increments. This allows crystallographic characterization of individual folia, individual foliated crystal units or/and only a few foliated crystal units. Indexing rate was at least 95%.

Both valves of *H. hyotis* were investigated. EBSD measurements were performed on cross-sections through the valves. We investigated three specimens in total. One specimen was used for scanning electron microscopy (SEM) imaging and two specimens were used for EBSD measurements. SEM imaging was performed only on fracture surfaces. Etched sample surfaces were not used to avoid imaging of etching artifacts.

2.3. Terminology

Subsequently, we describe the structural and crystallographic terms that we use in this study.

A crystal or crystallite is an entity that can have either a coherent 3-dimensional strictly periodic crystal lattice, which is only achievable theoretically, or it is an entity that comprises subunits separated from each other by small-angle grain boundaries [38]. These boundaries cause the subunits of the crystal or crystallite to be tilted with respect to each other. When tilted at low (<5°) angles, the subunits are termed mosaic blocks or mosaic domains of a crystal [38]. In EBSD data evaluations, crystals are defined by areas in EBSD maps that are contiguous within a chosen critical misorientation ω_{crit}, i.e., they contain mosaic blocks that are tilted by less than ω_{crit}.

A microstructure is an assembly of crystallites or crystals. We present microstructures with EBSD band contrast measurements and crystal orientation maps. EBSD band contrast is shown gray-scaled, and crystal orientation is shown in color, with the latter coding crystal orientations. We use inverse pole figure (IPF) and all-Euler coloring codes; the relevant coloring code is either given in the figure or indicated in the figure caption.

The texture or crystallographic preferred orientation of a polycrystalline material relates to the orientation pattern of the crystals comprising the material's microstructure. Texture patterns are illustrated with pole figures, which show either color-coded crystallographic axes or plane-normal orientation data or the contoured density distribution of crystallographic axes or plane-normal orientations. To display the density distributions, a half-width of 5° and a cluster size of 3° was chosen in the HKL CHANNEL 5 and AZTecCrystal software that were used for data evaluation. The half-width and cluster size regulate the spread of the poles over the surface of the projection of the orientation sphere.

The terms c-axes and a*-axes refer to the {001} and {100} sets of plane normals, respectively. As defined crystallographically, calcite has one c-axis and three symmetry-equivalent a*-axes. For a graphical view of this, please see Figure S1.

We use the term single-crystal-like crystal textures when we observe one cluster of poles for the c-axes and three clusters of poles for the three a*-axes in the calcite pole figure. A single-crystal-like texture with a graded distribution of calcite c- and a*-axes is present when the pole figure shows individual clusters for the c- and the three a*-axes orientations, where these clusters have an elongated appearance and display a curvilinear shape due to the recurrent gradual tilt of crystallographic axes distribution for each cluster.

A mesocrystal is defined as a mesoscopically structured crystal, consisting of submicrometer-sized crystallites that are organized within an individual mesocrystal with a crystallographic register [39–41].

We use the term crystal unit for morphological units, such as columns, prisms or foliated units that are crystals with an internal mosaic structure. For example, a foliated unit is a crystal with a mosaic structure that consists of an array of foil-shaped crystallites, the folia.

Axial textures are present when the orientations of the crystallites in the microstructure cluster around a common crystallographic direction (or plane-normal), and directions perpendicular to this texture axis are distributed homogeneously on a great circle around the texture axis direction. Other directions, which are at a smaller angle to the texture axis, are distributed homogeneously on small circles around the texture axis.

A spherulitic texture is given for calcite crystals when we observe, in the pole figures, a ring-like orientation distribution of c-axes and, in general, scatter for the three a*-axes orientations. Thus, in the case of a spherulitic texture, we observe strong co-orientation for calcite c-axes and either low or even lack of a*-axes co-orientation.

A spherulitic texture of a cluster of calcite crystals is present when the pole figure indicates that their preferred axes (usually c-axes) are distributed on the surface of a sphere and extend from a common origin. As EBSD maps are usually taken on sections of objects, an arbitrary section through a spherulite results in a ring-like distribution of c-axes on a small circle and, in general, scatter for the a*-axes orientations. Thus, in the case of a spherulitic or spherulite-like texture, we observe strong co-orientation for calcite c-axes and either low or even lack of a*-axes co-orientation.

A turbostratic texture is known for the arrangement of clay platelets when they settle in clay–water systems, such that there is a joint orientational axis of the platelet normal. However, the stacking involves random misorientations around the joint orientational axis [42,43]. Accordingly, for a turbostratic calcitic material, we expect to see pole figures like those of an axial texture, but, these have corresponding strongly structured distributions of calcite c- and a*-axes orientations in space. When calcite c- and a*-axes have a graded orientation distribution, we observe a ring-shaped orientation distribution for the c- and a*-axes in the pole figure.

We describe crystal co-orientation strength with (i) multiple uniform (random) distribution (MUD) values and, as a crystal is a three-dimensional object, with (ii) the angular spread of the three Euler angles, termed Euler 1, Euler 2, Euler 3, E1, E2, E3 angles, or angles with $\phi 1$, Φ, $\phi 2$ notation [44]. The MUD value is calculated from EBSD orientation data density distributions and is given for entire EBSD scans or for selected subsets of these. A high MUD indicates a high crystal co-orientation strength, while a low MUD indicates low co-orientation strength or a random, uniform, orientation distribution for MUD = 1. At a half-width of 5° and a cluster size of 3°, a perfect single crystal gives an MUD value above 700. The full angular spread of the three Euler angles is about 2° each for a calcite crystal precipitated from solution; the latter was measured with the SEM-EBSD system used in this study.

The degree of tilt or misorientation between crystals is obtained from EBSD measurements. We show the misorientation between crystals with (i) histograms displaying the relative frequency of misorientation angles or (ii) diagrams showing misorientation angle vs. distance from a reference point along a trajectory indicated as a to b, c to d, etc. We show misorientation between crystals and crystallites along trajectories that run either parallel to the length of a foliated unit or for trajectories that are perpendicular to the length of a foliated unit. For the misorientation of angle–distance diagrams, we give the cumulative misorientation angle, i.e., misorientation with respect to the initial reference point, termed also in this study as the first point.

For a better visualization and understanding of the texture of the foliated shell material, the Euler angles, ϕ1, Φ, ϕ2, were rotated in the virtual chamber of the CHANNEL 5 HKL and AZTecCrystal software for some EBSD scans and the corresponding pole figures. If the Euler angles are rotated at data evaluation, this is indicated either in the figure or is stated in the figure caption. At EBSD data acquisition the Euler angles are kept at zero, according to the used convention, while in this study and only for data evaluation, the Euler angles were rotated. Accordingly, the orientation of the specimen is changed virtually. Hence, the coordinate axes of the pole figures displaying the crystal orientations are no longer parallel to those of the shown map. If this is the case, it is indicated in the figure caption. For conventional EBSD acquisition and data evaluation, the Euler angles are set in the CHANNEL 5 HKL and AZTecCrystal software to $\phi1 = 0°$, $\Phi = 0°$, $\phi2 = 0°$. We give EBSD scans and corresponding pole figures evaluated with unchanged Euler angles ($\phi1 = 0°$, $\Phi = 0°$, $\phi2 = 0°$) and rotated Euler angles ($\phi1 = 35°$, $\Phi = -65°$, $\phi2 = 70°$). Nonetheless, at data acquisition, the Euler angles were set at $\phi1 = 0°$, $\Phi = 0°$, $\phi2 = 0°$ for all EBSD measurements presented in this contribution.

3. Results

The shell of the Ostreoidea consists of layers with diverse microstructures and hierarchical architectures [4]. The largest part of the shell by volume is formed of foliated calcite and spans across several hierarchical levels. Figure 1 shows, for the foliated shell of the gryphaeid *Hyotissa hyotis*, the different microstructural levels that we identified with the analytical techniques used in this study. The foliated shell layer consists of lath-shaped crystals with arrowhead endings (A). These are about 1 to 2 µm wide, about 200 to 300 nm thick and about 20 to 25 µm long. Upon juxtaposition, the laths tend to form 10 to 20 µm wide sheets, foils or folia (white stars in Figure 1B); these overlap slightly laterally and vertically in the *H. hyotis* shell (C). Arrays of folia are arranged, more or less, in parallel (Figure 1D) and form foliated units/entities (see gray-scaled band contrast measurement image in Figure 1E). We distinguish individual foliated units by differences in calcite c- and a*-axes orientation, relative to the c- and a*-axes orientation of the neighboring foliated unit (see, for crystal orientation colored, EBSD measurement image in Figure 1F,G).

Figures 2, 3 and S2 show the microstructure, the mode of calcite c- and a*-axes orientation (the texture) and misorientation angle diagrams of trajectories that run either parallel or perpendicular to the length of a foliated unit for individual foliated units. We observe (i) the graded nature of calcite c- and a*-axes orientation (see the pole figures in Figures 2 and S2) and the smooth change in colors in Figures 2 and S2; (ii) the very smooth increase in misorientation, relative to the first point on the trajectory for trajectories that run parallel to the length of the foliated unit (Figures 2, 3 and S2); (iii) the rather irregular increase in misorientation relative to the first point along trajectories that run perpendicular to the length of the foliated unit (Figures 2 and 3); and (iv) the similar misorientation gradient for the misorientations along the different trajectories (Figures 2, 3 and S2).

The calcite of individual folia (Figure 4A) is very co-oriented. We calculate an MUD value of more than 700 and an angular spread in misorientation of 2 to 3° for the three Euler angles. For comparison, we give the MUD value and angular spread of misorientation of the three Euler angles of a calcite single crystal precipitated from a solution (Figure 4B). We find very similar MUD values and angular spread in misorientation for the three Euler angles (compare the results in Figure 4A with those given in Figure 4B). The cumulative misorientation of an individual folium is up to 2.6°. The degree of misorientation between adjacent folia is below 1°. For the example shown in Figure 4C, the misorientation between adjacent folia is 0.7°. Accordingly, for two adjacent folia, the MUD value is above 700. Misorientation within one of the folia, as shown in Figure 4C, goes up to 1.6°. The degree of misorientation between four adjacent folia (Figure 4D) scatters up to 1.5°. It is slightly increased, relative to the misorientation of 0.7° between two adjacent folia; nonetheless, it should be noted that the misorientation between four adjacent folia is still not high. The MUD value for the latter array of folia is 650 (Figure 4D). In essence, when regarding stacks of folia, we find that adjacent folia are very co-oriented and that the calcite of an array of folia is still close to being single-crystalline (e.g., the MUD value of a stack of folia is 650).

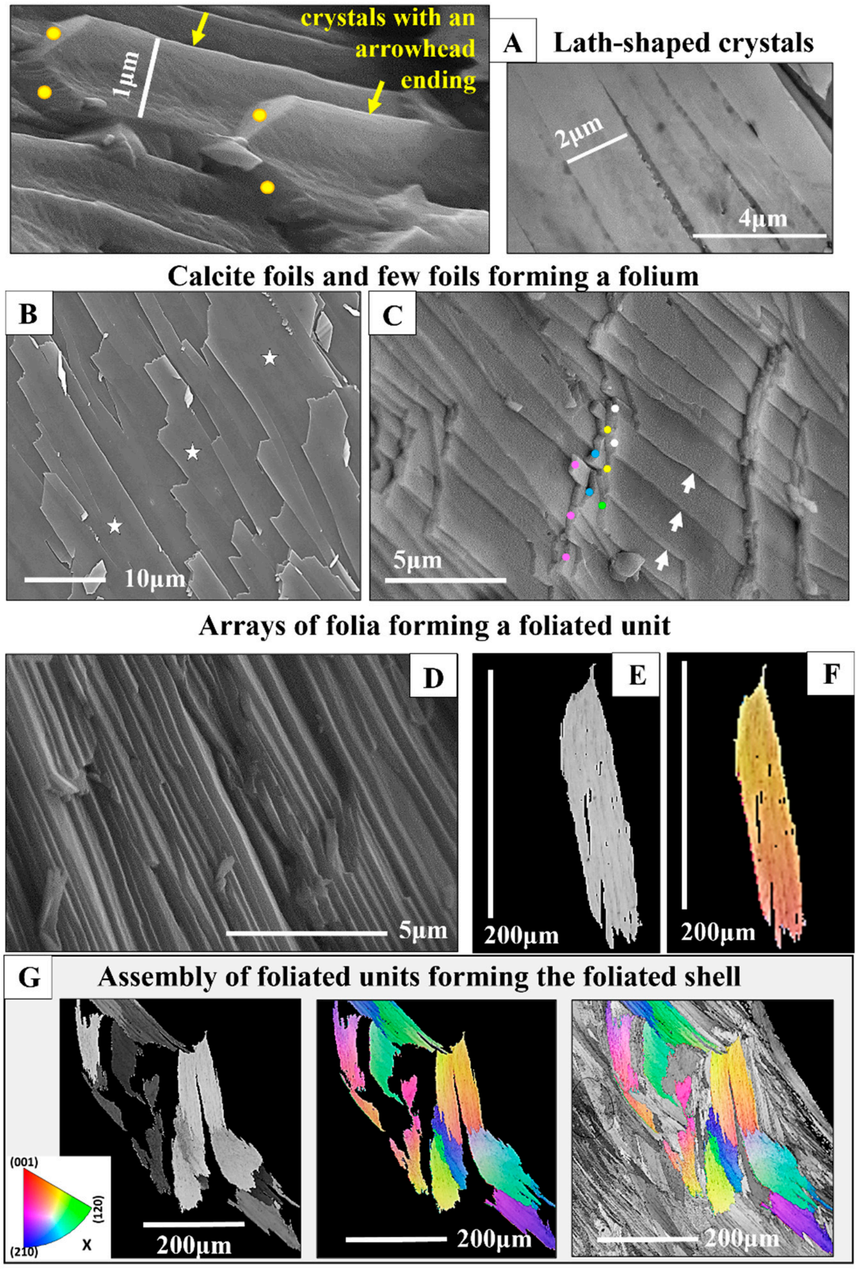

Figure 1. The hierarchical organization of the foliated shell layer of *H. hyotis*. The latter is formed of lath-shaped crystals having arrowhead endings (yellow dots) (**A**) that join laterally and form a folium (white stars in (**B**)). Two to three folia overlap horizontally (white arrows in (**C**)) and vertically (colored dots in (**C**)) and form a foliated unit (**E**,**F**). Assemblies of foliated units (**F**,**G**) comprise the foliated shell layer. (**A**–**D**): BSE micrographs. (**E**) and grey-scaled image in (**G**): EBSD band contrast measurement image. (**F**) and colored image in (**G**): Pattern of calcite orientation, color-coded for crystal orientation, in an individual foliated unit (**F**) and in assemblies of foliated units (**G**).

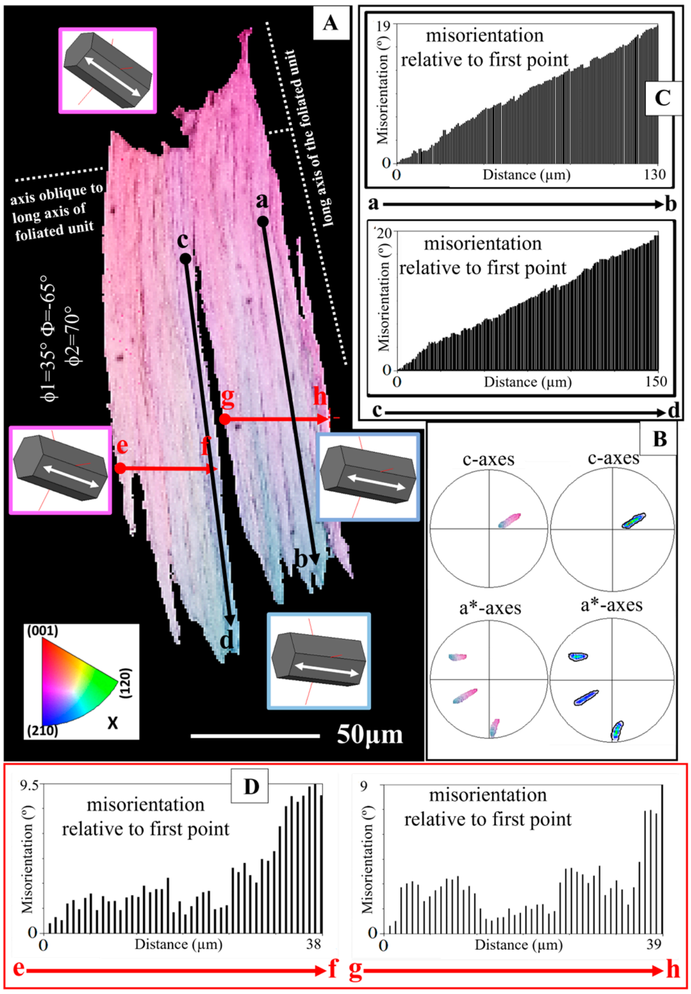

Figure 2. The microstructure, texture and mode of crystal misorientation of a foliated unit of *Hyotissa hyotis*. (**A**) EBSD map of the foliated unit, color-coded for crystal orientation; the entire EBSD scan is given in Figures 3A and 5B,D. The striation of the foliated unit is well visible, indicating the stacked arrangement of the comprising folia and the steady change in color with the length, and perpendicular to the length of the striation. Sketched crystals and the white arrows show calcite crystal and calcite c-axis orientation, respectively. As the color of the foliated unit codes for crystal orientation, we observe for the foliated unit a steady change in calcite orientation: (i) along the length of the foliated unit (white dashed line in (**A**)) and (ii) perpendicular to the latter across many adjacent folia (white dashed line in (**A**)). (**B**): c- and a*-axes pole figures, giving the orientation data points and their density distributions for the foliated unit shown in (**A**). We see elongated clusters for the c- and the three a*-axes. This demonstrates the graded distribution in c- and a*-axes orientation for the calcite of the foliated unit shown in (**A**). (**C**,**D**): Crystal misorientation along trajectories parallel to the length of the foliated unit (a to b and c to d, in black in (**A**,**C**)) and perpendicular to the latter (e to f and g to h, in red in (**A**,**D**)). We give the cumulative misorientation in the misorientation angle–distance diagrams, hence, misorientation relative to the first point along the trajectory. For the trajectory that runs parallel to the length of the foliated unit (given in black), we find a very smooth increase in misorientation angle, relative to the first point, while for the trajectory that is oblique to the length of the foliated unit, which crosses many adjacent folia (given in red), we still observe the tendency of an increase in cumulative misorientation angle; however, the progression of the increase in misorientation angle is markedly irregular and very different from the progression of the misorientation angle along the trajectory that is parallel to the length of the foliated unit. At EBSD data evaluation, the Euler angles were rotated in the virtual chamber from $\phi 1 = 0°$, $\Phi = 0°$, $\phi 2 = 0°$ (the conventional Euler angle setting at measurement and data evaluation) to $\phi 1 = 35°$, $\Phi = -65°$, $\phi 2 = 70°$ (for a better visualization of the foliated texture, rotated Euler angle setting, only at data evaluation).

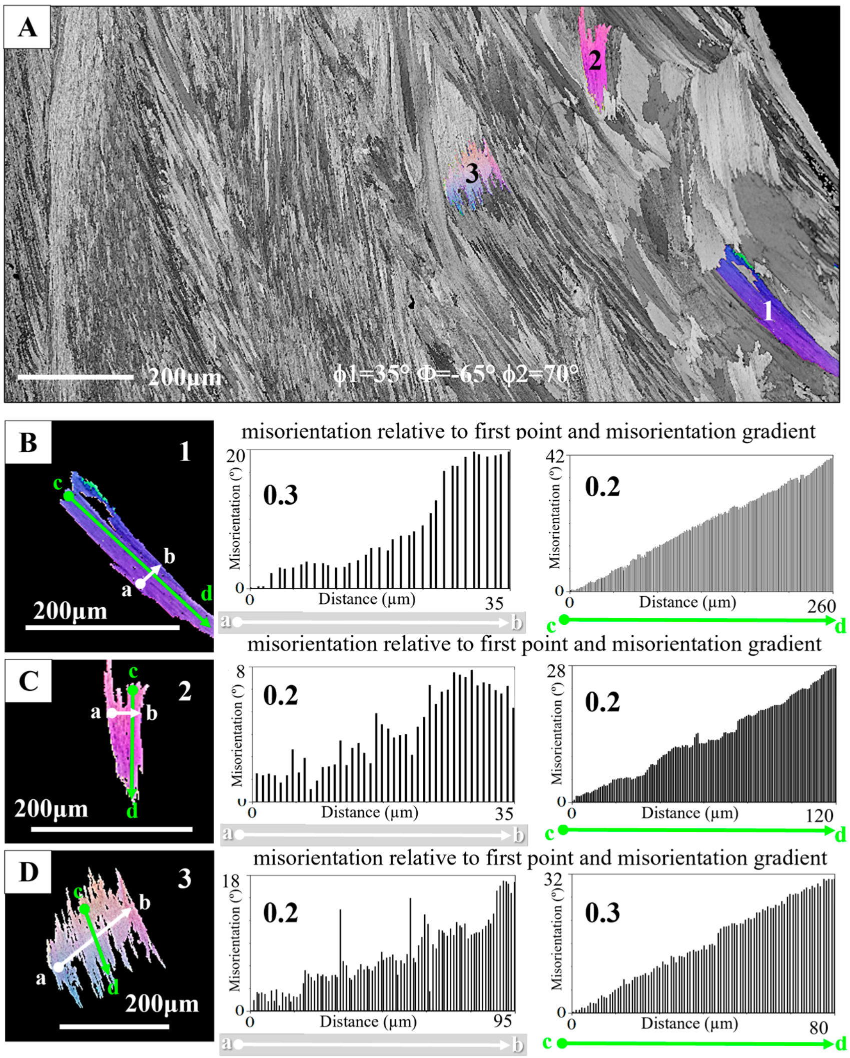

Figure 3. Misorientation angle patterns between crystals along differently oriented trajectories for three foliated units of the *Hyotissa hyotis* shell. (**A**): EBSD band contrast measurement image (gray-scaled) of a shell portion of *H. hyotis*. In color, depicting crystal orientation, are four selected foliated units (numbered 1 to 3). (**B**–**D**): Misorientation angle–distance diagrams and misorientation gradients (the numbers in the misorientation diagrams) for trajectories a to b and c to d. For each foliated unit, we show the misorientation angle change for two trajectories: parallel and perpendicular to the length of the foliated unit. We give cumulative misorientation angle change, hence, misorientation angle, relative to first point. Depending on the orientation of the trajectory, we see significant differences in the smoothness of the progression and an increase in misorientation angle. Along trajectories that run parallel to the length of the foliated units (trajectories drawn in green), the increase in misorientation angle with distance away from the first point on the trajectory is very smooth, in contrast to trajectories that run orthogonal to the length of the foliated units (trajectories drawn in white). At EBSD data evaluation, the Euler angles were rotated in the virtual chamber from $\phi 1 = 0°$, $\Phi = 0°$, $\phi 2 = 0°$ (the conventional Euler angle setting at measurement and data evaluation) to $\phi 1 = 35°$, $\Phi = -65°$, $\phi 2 = 70°$ (for a better visualization of the foliated texture, rotated Euler angle setting, only at data evaluation). For color legend, please see Figure 2.

In Figure 5A–D, we show, for an EBSD scan, the EBSD map and corresponding pole figures, including the EBSD data evaluation with an Euler angle setting of zero (Figure 5A,B) and a Euler angle setting of $\phi 1 = 35°$, $\Phi = -65°$, $\phi 2 = 70°$. Figure 5A,C show the difference in sample orientation in the virtual chamber, Figure 5B,D show the difference in color (that codes for crystal orientation) in the EBSD map and, in particular, in the c- and a*-axes density distributions. Please keep in mind that the color code has not been changed for the maps shown in Figure 5B,D; the difference in color is due to the rotation of the sample and its crystals in the virtual chamber. We observe a ring-shaped distribution of calcite c- and a*-axes (Figure 5C); thus, for the assembly of foliated crystals, there is a very specific texture. Figure 5E,F highlights, with the EBSD map and corresponding pole figures, how this texture pattern evolves. We describe the latter with the structures observed for large foliated units. The EBSD map in Figure 5E depicts a portion of a large foliated unit (see green rectangle in Figure 5F). We observe the structuring of the foliated unit into two subunits, nonetheless, with the subunits being strongly interwoven. We find two main crystal orientations in the EBSD map, one visualized with red to purple colors and the other with light to dark blue colors. Note the very smooth transition in color (and, thus, pattern of crystal orientation) between red to purple colors and light to dark blue colors (EBSD map in Figure 5E). In the corresponding pole figure, we see clusters for the c-axes and individual clusters for the three a*-axes. However, we also see the substructuring of the c- and a*-axes clusters. In the foliated unit shown in Figure 5F, crystal 1, an adjacent foliated unit is added (shown with yellow-green colors in Figure 5(F-2)). Further c- and a*-axes clusters are present in the corresponding pole figure (see pole figure for unit 2 in Figure 5F), and we see now in the pole figure the start of a ring-shaped c- and a*-axes orientation distribution pattern. Note that the foliated unit shown with yellow and green colors in Figure 5F is also structured and consists of two strongly interdigitating subunits (crystal orientation of these shown with yellow and green colors). The addition of further adjacent foliated units (unit 3 in Figure 5F) results in the addition of further c- and a*-axes clusters to the pole figure and a more complete development of the c- and a*-axes' ring-shaped orientation distribution (see pole figure for unit 3 in Figure 5F). Hence, the foliated unit complex within the white dashed lines in Figure 5D,F is formed of at least three (a, b, c) adjacent foliated units. These interlink strongly, and each of these consists of at least two different subunits with slightly different c- and a*-axes orientations.

Figure 6 shows, for a further EBSD scan taken on the large foliated units, the ring-shaped mode of calcite c- and a*-axes orientation (Figure 6A,B). The strong co-orientation of both crystallographic axes of the calcite and the presence of c-axes orientation clusters within the c-axis orientation ring are well visible in the pole figures. We subdivided the latter into 10 different clusters (Figure 5C) and highlighted these with EBSD maps and the corresponding pole figures. The stretched distribution of calcite a_1*-, a_2*- and a_3*-axes (blue arrows in pole figure for foliated subunit 1 in Figure 6C), the internal structuring of the a*-axes maxima by further clusters (black arrows in the a*-axis pole figure of foliated subunit 1 in Figure 6C) and the graded mode of orientation distribution, as shown in Figure 6 for the a*-axes and the foliated subunits, are well visible in the contoured version of the pole figures (see for all a*axes pole figures showing the orientation data points the smooth transformation from one color into the other).

Figure 7 shows pole figures for different calcite plane directions for two EBSD measurements on *H. hyotis* foliated calcite. For all EBSD maps shown, we observe the {100}, {001}, {104}, {105}, {106}, {107}, {108}, {1 0 18} and {1 0 20} pole figures. The {001} and {100} are coincident with the c- and a*-axes orientation of the calcite (see also Figure S1). We see the ring-shaped distribution of calcite c- and a*-axes orientations and also clusters in or near the center of the {104}, {105}, {106}, {107} and {108} pole figures. The strongest clusters we find are for the {105} and {106} plane normal directions. Thus, the texture of the foliated shell of *H. hyotis* is the result of the specific cone-shaped c- and a*-axes orientation distribution that are displayed with a ring in a 2D image and a cone axis near the {105} and {106} poles. As the arrowhead endings of the lath-shaped crystals point to inner shell surface [11,13,22], the planes with the {105} and {106} plane normal are, more or less, parallel to inner shell surface. The latter described texture pattern does not develop with foliated shell growth. It is an intrinsic characteristic that is already present in the formation of the very first crystals (Figure 8). It is the result of structural material formation out of lath-shaped crystals with arrowhead endings (Figure 1A), with the arrowheads pointing towards the growth direction of the calcite and, due to geometrical constraints, with the tip of the arrowhead crystal being bordered by flat planes. Figures S3 and S4 show the microstructure and texture of the foliated shell of other gryphaeids (*Hyotissa mcgintyi* (H. W. Harry, 1985), *Neopycnodonte cochlear* (Poli, 1795)) and some ostreid (*Magallana gigas* (Thunberg, 1793), *Ostrea stentina* Payraudeau, 1826, *Ostrea edulis* Linnaeus, 1758) species with EBSD maps and pole figures. For these species, we find a similar microstructure for the foliated shell and a texture pattern determined by c- and a*-axes orientation rings around the pole near the {105} and {106} plane normals.

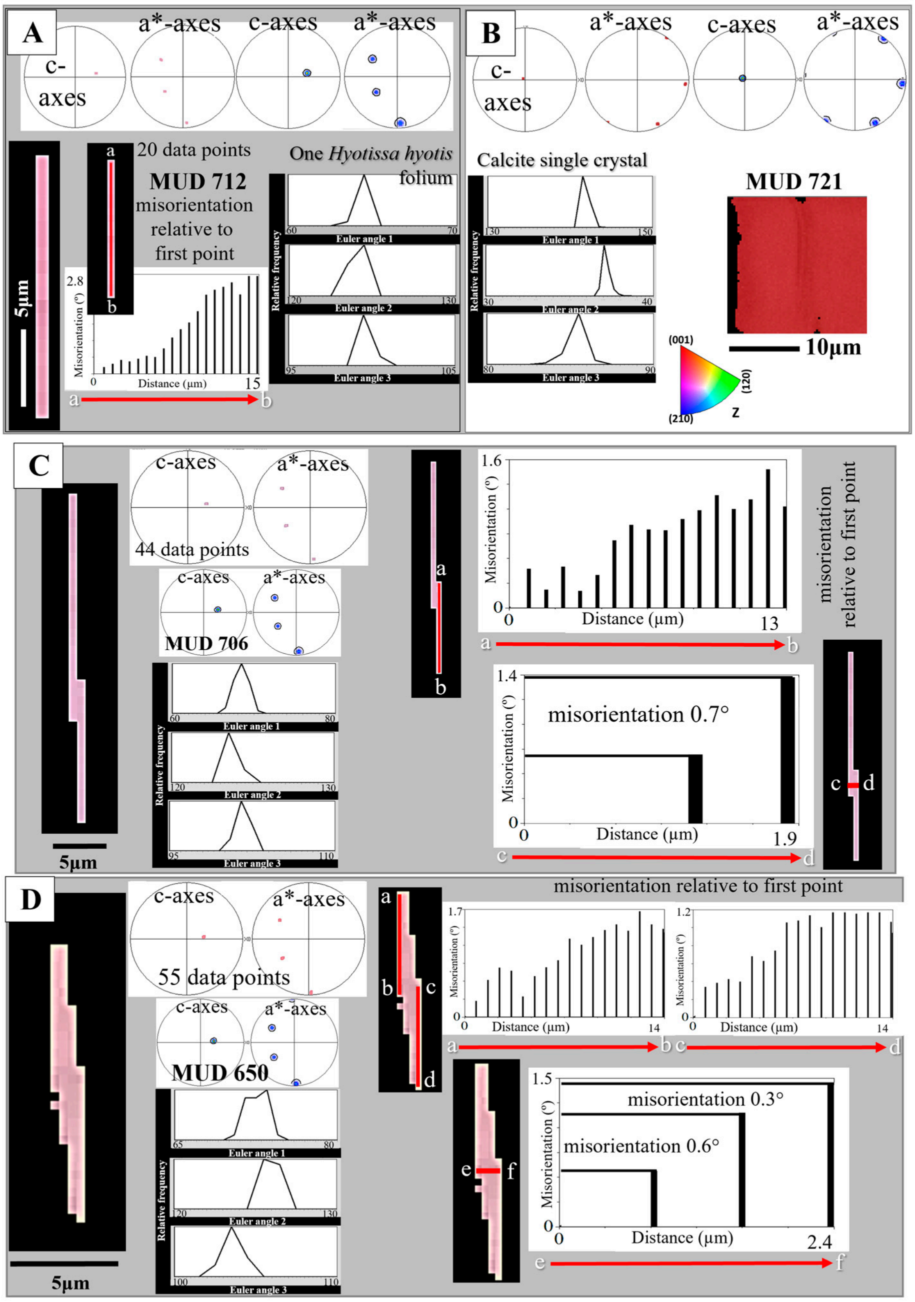

Figure 4. The degree of calcite c- and a*-axes co- and misorientation in a folium (**A**) and in two (**C**) and three (**D**) adjacent folia. (**A**–**D**) Crystal orientation color-coded EBSD maps and the corresponding pole figures given in either calcite c- and a*-axes orientation data or their density distribution. Furthermore,

we show in A to D misorientation angle–distance diagrams along trajectories a to b, c to d and e to f relative to the first point on the trajectory. We give MUD values for the shown EBSD scan in the figure and relative frequency–Euler angle diagrams to demonstrate the EBSD scan given in the figure and the spread in the three Euler angles (Euler angle 1, Euler angle 2, Euler angle 3). We find that the calcite of individual folia is very co-oriented (**A**) and very similar to the calcite of a crystal grown from solution (**B**). As the degree of misorientation between adjacent folia is very low, misorientation angles scatter between 0.3° and 0.7° (**C**,**D**), and the calcite of a foliated unit is also strongly co-oriented. Misorientation angle along the length of a folium ranges up to two degrees (**A**,**C**,**D**); misorientation angle between very few adjacent folia ranges in total up to 1.5°. Hence, the calcite in individual folia and a foliated unit is very co-oriented.

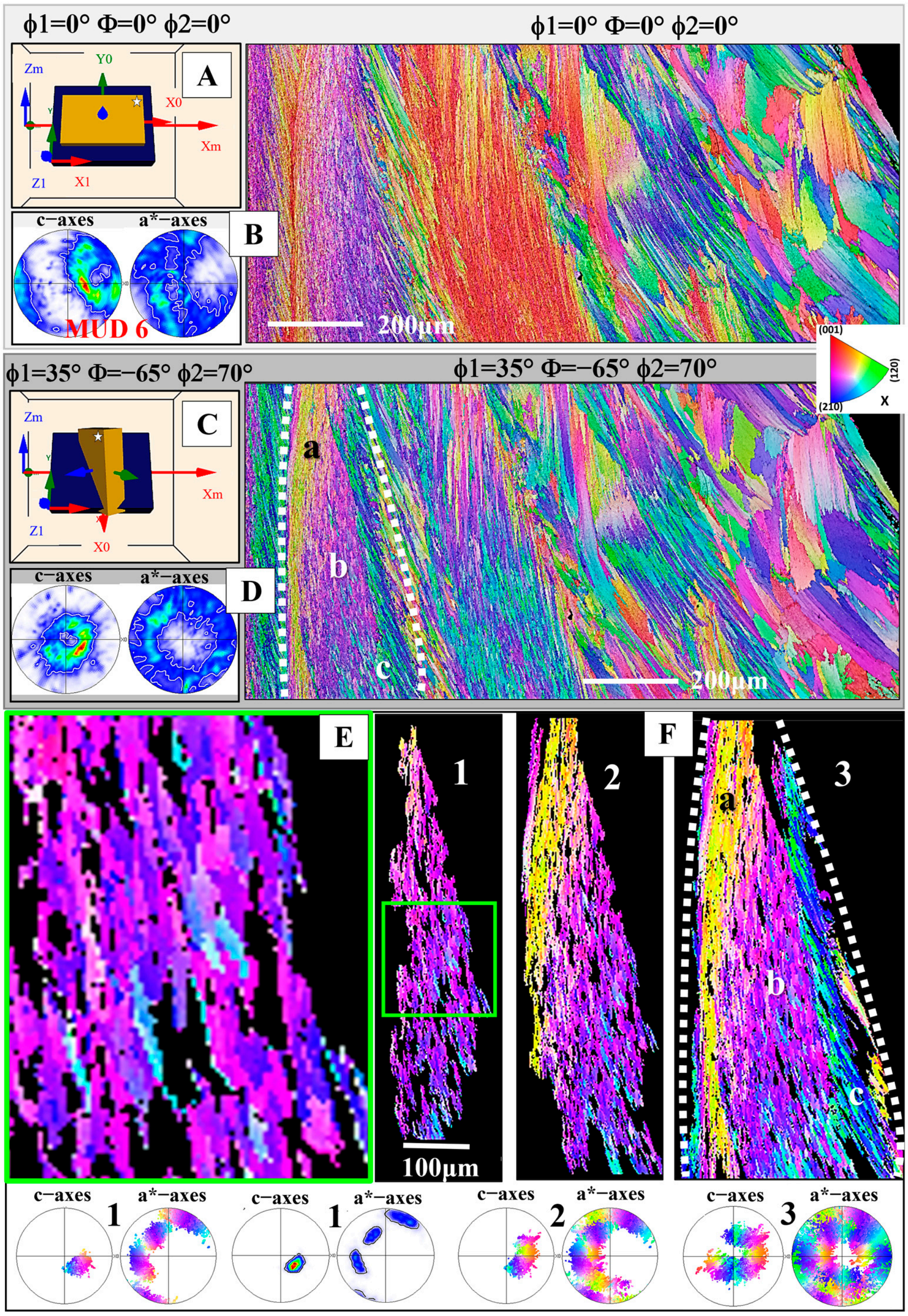

Figure 5. The microstructure, texture and crystal co-orientation strength (MUD value) of an EBSD scan that covers small and large foliated units that form the foliated shell of *Hyotissa hyotis* (**B**,**D**). The

scan extends from the inner shell surface into the foliated shell layer. The colors in (**B**,**D–F**) code for calcite orientation. We find small and large foliated units. Crystal co-orientation strength is very low; we calculated an MUD of 6 for the entire measurement (**B**,**D**). For a better understanding of the c- and a*-axes texture pattern, at EBSD data evaluation, the three Euler angles were rotated in the virtual chamber from $\phi1 = 0°$, $\Phi = 0°$, $\phi2 = 0°$ (**A**), the conventional Euler angle setting at measurement and data evaluation, to $\phi1 = 35°$, $\Phi = -65°$, $\phi2 = 70°$ (**C**), a rotated Euler angle setting for data evaluation (**A**–**D**). The colors in the scans shown in (**B**,**D**,**F**,**G**) code for crystal orientation; note that the difference in color between (**B**,**D**) is not due to a change in color code but to a change in Euler angles at data evaluation. When the Euler angles are rotated, we observe, for both crystallographic axes of the calcite, a ring of c- and a*-axes orientation (**D**). (**E**,**F**): The microstructure and texture of an interlinkage of adjacent large foliated units and the c- and a*-axes orientation rings in the corresponding pole figures. (**E**): EBSD map showing a portion of a large foliated unit; the position of the EBSD scan is indicated with a green rectangle on the foliated unit no. 1 in (**F**). We observe light to dark blue and red to purple colors in the map and the corresponding pole figure, hence two sets of calcite orientations. The corresponding texture pattern shows that the c- and a*-axes orientation clusters are substructured and consist of at least two c- and two a*-axes orientation maxima. These correspond to the calcite orientations shown in dark to light blue and red to purple colors in the EBSD map in (**E**). Nonetheless, we find clusters for the c- and the three a*-axes orientations. The foliated unit no. 1 in (**F**) is flanked by other foliated units (no. 2 and no. 3. in (**F**)). These also have substructured c- and a*-axes clusters in the pole figure and consist of subunits with slightly different orientations. Hence, the shell portion framed with white dashed lines in (**D**,**F**) comprises at least three large interdigitating foliated units (a, b, c in (**D**,**F**)); each of these have slightly different orientation, and each of these foliated units consists of at least two interdigitating subunits, with these having also slightly different orientations. The assembly and interdigitation of adjacent foliated crystal units and the interdigitation of their subunits create a very specific texture pattern, forming orientation rings in the c- and a*-axes pole figures (see pole figures 1, 2, 3 in (**E**)).

Figure 9 highlights c- and a*-axes and {105}, {106} plane normal orientation data for three c-axis maxima of the c-axes orientation ring. The maxima were taken from different parts of the c-axis orientation ring. We observe (i) the internal structuring of the three a*-axes by further orientation maxima; (ii) the gradual change in a*-axis orientation for the three a*-axes; (iii) the rotation of {105} and {106} plane orientation with c- and a*-axes rotation in the c-axis ring; and (iv) the orientation of one {105} and {106} plane orientation cluster pointing out of the plane of view and being parallel to inner shell surface.

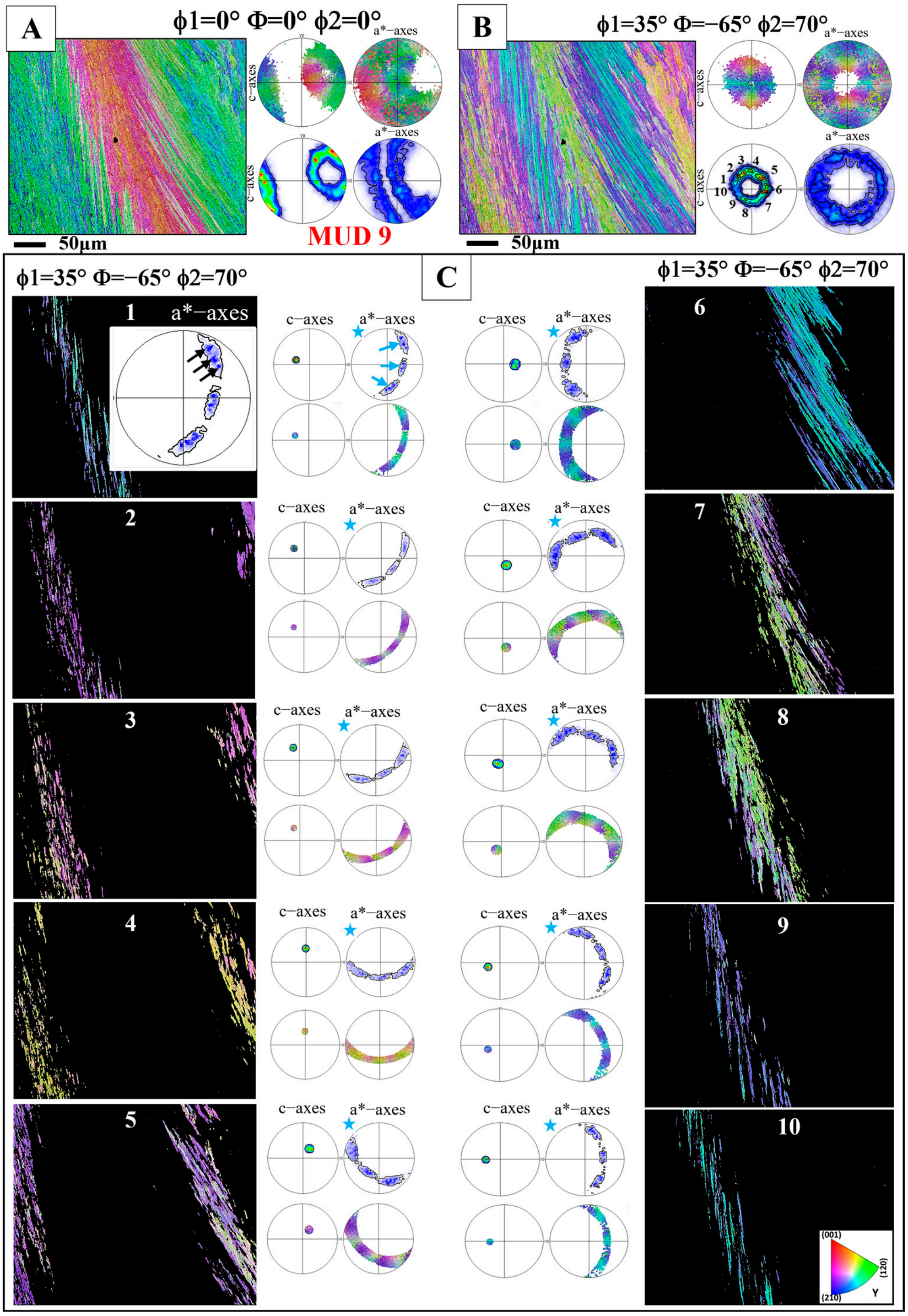

Figure 6. The c- and a*-axes orientation clusters comprising the c- and a*-axes orientation rings, visible in the corresponding pole figures. (**A**,**B**): EBSD measurement taken on the foliated shell portion of *Hyotissa hyotis*. For a better visualization of the texture pattern, the three Euler angles were rotated in the virtual chamber from ϕ1 = 0°, Φ = 0°, ϕ2 = 0° (the conventional Euler angle setting at measurement and data evaluation) to ϕ1 = 35°, Φ = −65°, ϕ2 = 70° (the rotated Euler angle setting at data evaluation). (**C**): We observe (i) a ring in c-axis and a*-axes orientation, (ii) consisting of c- and a*-axes orientational clusters (clusters 1 to 10), and (iii) the graded nature of axes orientation (blue star at density distribution pole figure for clusters 1 to 10) and blue arrows in a*-axis pole figure for crystal cluster 1. We also observe (see insert in map for crystal cluster 1) the hierarchical organization of a*-axes orientation. For each a*-axis, we find further clusters of a*-axis orientation; see black arrows in the insert in crystal cluster 1. Nonetheless, for the measurement shown in (**A**,**B**), we find a low crystal co-orientation strength, and we calculate an MUD value of 9.

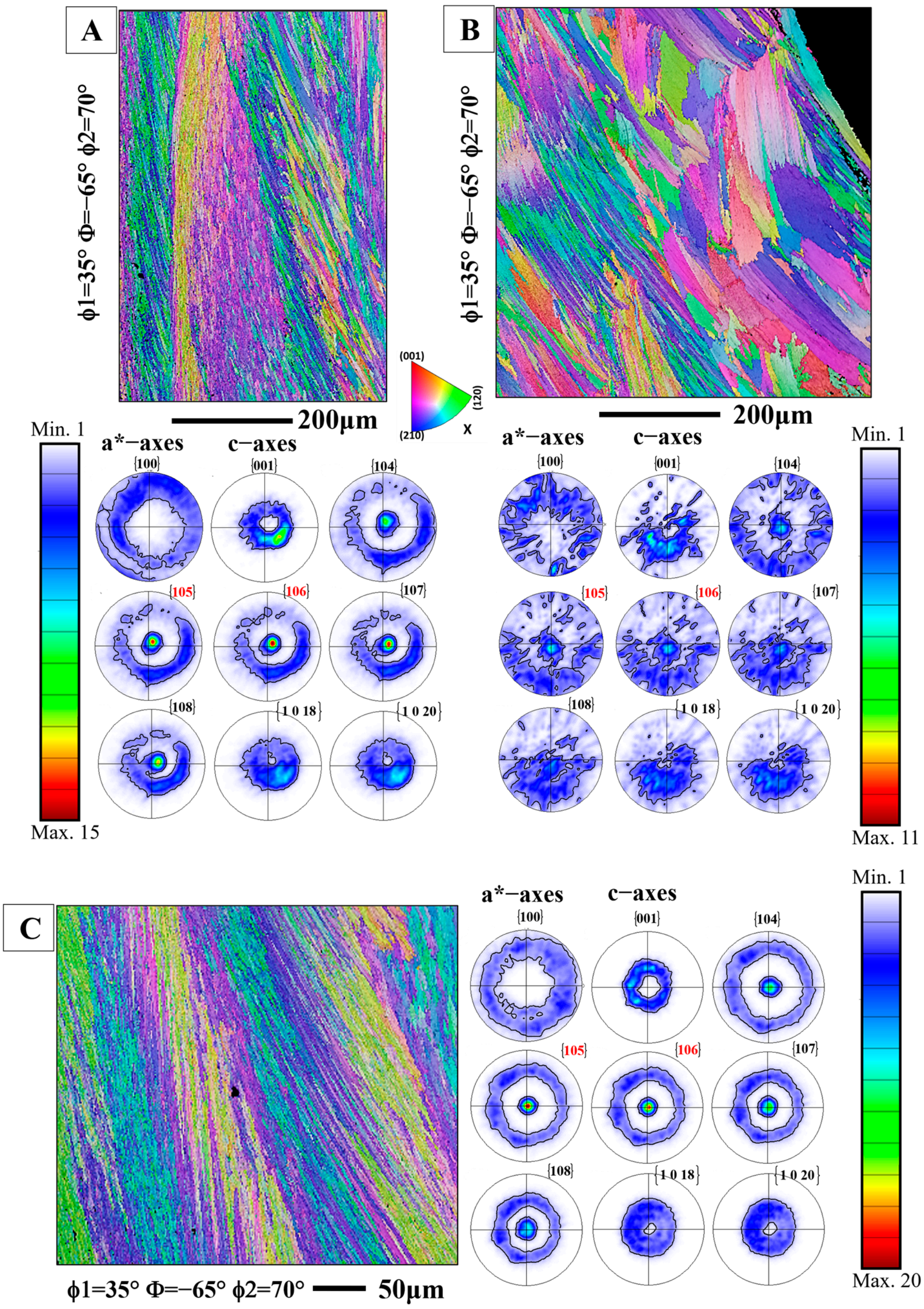

Figure 7. Pole figures of various calcite orientations in the foliated shell layer of *Hyotissa hyotis*. EBSD measurements and corresponding pole figures scanning over large (**A**,**C**) and small (**B**) foliated units of the *H. hyotis* shell. The three Euler angles were rotated in the virtual chamber from ϕ1 = 0°, Φ = 0°, ϕ2 = 0° to ϕ1 = 35°, Φ = −65°, ϕ2 = 70°. We show with the {100}, {001}, {104}, {105}, {106}, {107} and {108} pole figures.We find a ring (cone-shaped distribution) in in c-axes {001} and the a*-axes {100} around a pole near {105} and {106} plane normal orientations. Further, we find strong maxima in the rings of the c-axes orientations, as well as in the {105} and {106} pole figures. Thus, these are the principal orientation directions in the foliated shell. The measurement in (**B**) covers many misoriented foliated units, while the measurement in (**A**) covers part of a few adjacent large foliated units. Nonetheless, we find the same texture pattern for the large and small foliated units.

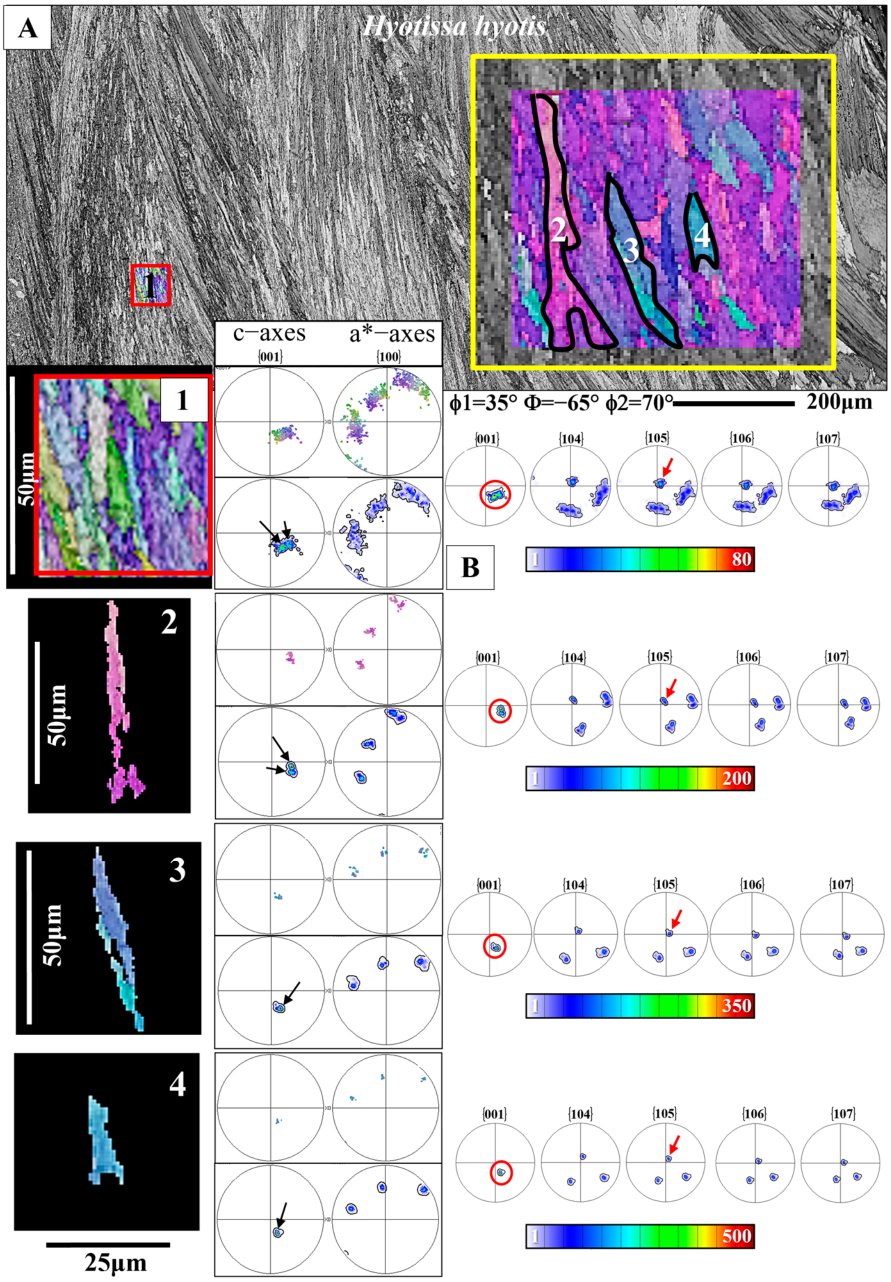

Figure 8. The texture of very few crystals of a large foliated unit ((**B**): crystal assemblies 1 to 3 and crystal 4). (**A**): Band contrast measurement image of the entire measurement, with the position of EBSD map 1 shown in (**B**) indicated by a red rectangle and positions of the remaining EBSD maps indicted by the yellow rectangle. (**B**)—EBSD map 1: assembly of a few crystals; (**B**)—EBSD map 2: assembly of three to four crystals; (**B**)—EBSD map 3: assembly of two crystals; (**B**)—EBSD map 4: one crystal. We show the pole figures for {001}, {100}, {104}, {105}, {106} and {107}. The black arrows in the c-axes pole figures point to the internal structuring of the map 1, map 2, map 3 and map 4 c-axis clusters. The red circle indicates that for all subsets 1 to 4 we observe the {001} plane normal directions. The red arrows for subsets 1 to 4 indicate that we find in cases a strong peak in the pole figure for the {105} plane normal direction. For both, the map 1 and map 2 c-axes clusters we find two internal maxima, for the map 3 and the map 4 clusters only one c-axis maximum. Irrespective of whether we regard a few foliated crystals (EBSD map 1 in (**B**)) or just one crystal (EBSD map 4 in (**B**)), we find strong maxima in {001}, the c-axes, and in {105}. Thus, generation of distinctive {105}, {106} plane normal directions is intrinsic for the calcite that generates the foliated microstructure. The formation of {105} and {106} plane directions is the result of the foliated crystals, with the laths having arrowhead endings. See the yellow dots on the planes of a lath-shaped crystal in Figure 1A. These

planes are the planes with the {105} and {106} directions. For both, the map 1 and map 2 c-axes clusters we find two internal maxima, for the no. 3 and the no. 4 clusters only one c-axis maximum. The red circle indicates that for all subsets 1 to 4 we observe the {001} plane normal directions. The red arrows for subsets 1 to 4 indicate that we find in cases a strong peak in the pole figure for the {105} plane normal direction.

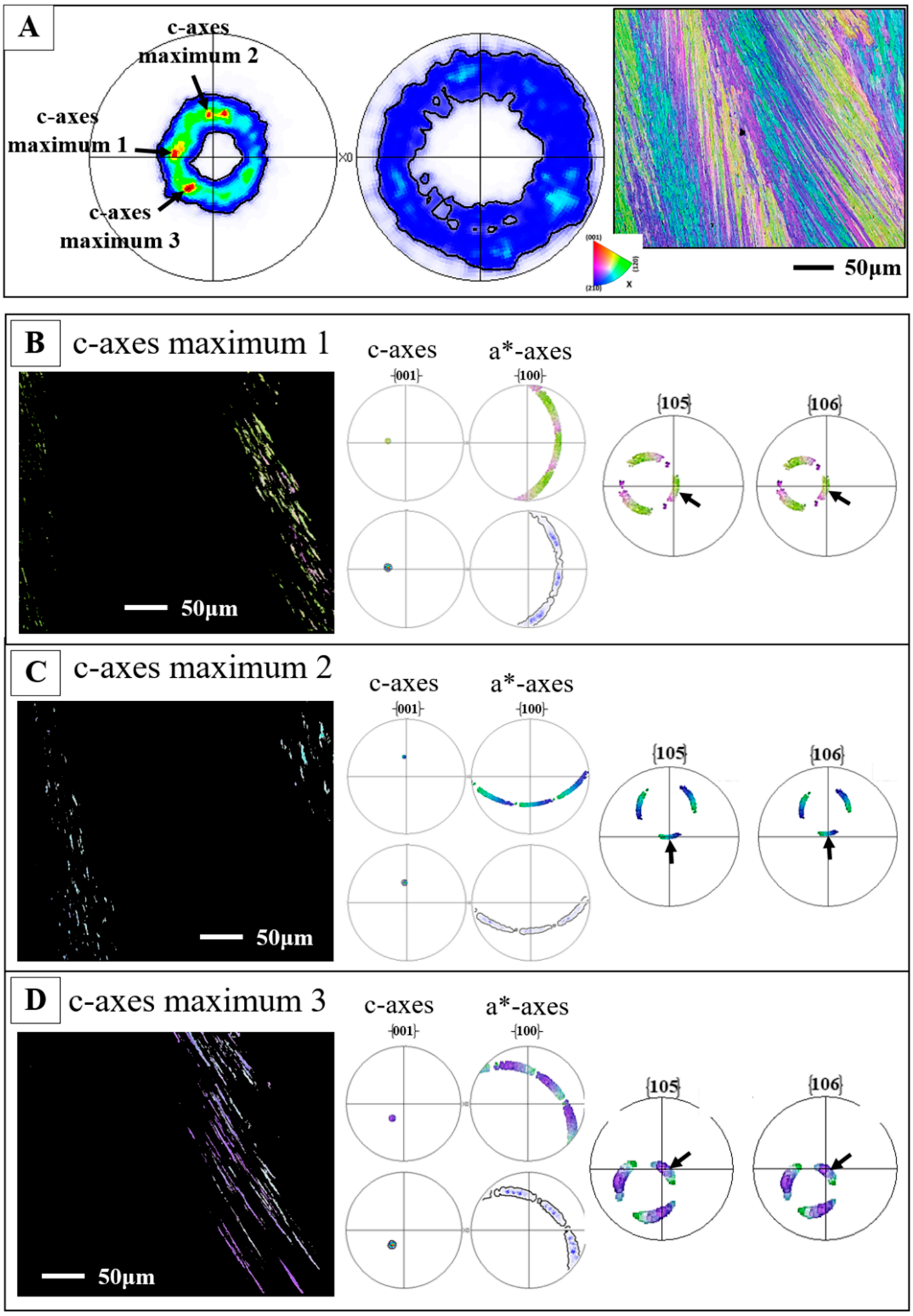

Figure 9. (**A**) EBSD map and pole figures showing the ring of c-axes orientation. (**B**–**D**): Microstructure and texture of prominent calcite c-axes maxima and the corresponding {001}, {100}, {105} and {106} pole figures. See the different orientation of the three selected c-axes maxima from the ring of c-axes orientation (**A**). The black arrows in (**A**) point to the presence of c-axes clusters on the c-axes orientation ring. The black arrows in (**B**–**D**) point to the presence of the {105} and {106} plane normal orientations. For the corresponding a*-axes distributions we observe an almost even distribution on a great circle and forthe {105} and {106} plane orientations; irrespective of their change in orientation, some plane normal in the center of the pole figure.

4. Discussion

SEM images and EBSD maps of studies from the last few decades show that the crystals of skeletons and skeletal elements of biocarbonate-secreting marine organisms are assembled with many microstructure patterns. Nonetheless, XRD and EBSD measurements show that, for the many microstructures, we find only a few major texture patterns [4,28,29,45,46]. The main texture modes that we find today for biocarbonate crystals produced by marine organisms can be addressed as being either (i) a single-crystal-like texture, (ii) an axial texture, (iii) a spherulitic texture or (iv) a polycrystal texture with almost no preferred orientation [4,28,29,46–48]. For the definition of the textures, see the Terminology Section in the Materials and Methods. In our study, we use the terms 'microstructure' and 'texture' according to the terminology used in material science [44]. XRD and EBSD studies of the last four decades have shown that axial textures dominate the texture patterns of modern Ca-carbonate biocrystals and microstructures. It has further been shown that the pure end-members of the modes of crystal assembly patterns, a single crystal-like texture and a texture without any preferred orientation of the crystallites, even in cases where the crystals are secreted for reinforcement of a biological structure (e.g., the cuticle of isopods), are, in general, not developed for biocarbonate hard materials [46,49]. This is in contrast to man-made materials, where we find the generation of both (i) single crystals and (ii) polycrystals without any preferred orientation (e.g., [46] and references therein). In the case of Ca-biocarbonate structural materials, the Ca-carbonate hard tissue (or assembly of biocrystals) that comes closest to the pure end-members of the textures given above are, for a single crystal texture, the sclerites of Caudofoveata *Falcidens gutturosus* (Kowalevsky, 1901), *Scutopus ventrolineatus* (Salvini-Plawen, 1968) [50], Solenogastres *Dorymenia sarsii* (Koren & Danielssen, 1877), *Anamenia gorgonophila* (Kowalevsky, 1880) and *Simrothiella margaritacea* (Koren & Danielssen, 1877) [51]. For a polycrystalline texture without preferred orientation, the closest examples are the spicules of the polyplacophoran species *Acanthopleura vailantii* (Rochebrune, 1882) [52] and the hard tissue of the stony coral *Porites* sp. (Link, 1807) [53]. The hard tissue of all these examples consists of biologically secreted aragonite.

4.1. What Is the Texture Pattern of the H. hyotis Foliated Calcite Microstructure?

4.1.1. The Calcite c- and a*-Axes Orientations in the Pole Figures

The foliated microstructure of bivalve shells has been extensively investigated via light microscopy and SEM imaging; excellent reviews of structural characteristics and the previous literature are given by Galtsoff [23], Taylor et al. [12] and Carriker et al. [2]. Crystallographic details of Ostreoidea foliated shell crystals, obtained from XRD and EBSD measurements, are given by different authors [6,11,22,54]. These studies present significant knowledge on the orientation of the lath-shaped crystals within the foliated shell by deciphering the orientation of many plains of a lath crystal, relative to the shell surface. Nonetheless, the texture of the foliated calcite is still little addressed and will subsequently be discussed for the gryphaeid species *Hyotissa hyotis*.

The texture pattern of Ostreoidea foliated calcite is very specific and outstanding when compared to the textures of other Ca-carbonate hard tissues produced by bivalved marine organisms The outcome of the EBSD data evaluation detailed in this study is that the foliated texture of *H. hyotis* is the result of the shape of the foliated crystals (the laths), their arrowhead ending as well as the strongly structured organization of the lath-shaped crystals for the generation of folia. Furthermore, the foliated texture results from the strongly structured, vertically and laterally overlapping, organization of folia for the formation of a foliated unit. Thus, for the generation of the foliated calcite texture pattern, two main microstructural characteristics need to be combined: (i) the production of laths with a specific morphology and a specific ending and (ii) their very highly structured mode of organization in the foliated unit.

The strong structuring of overlapping, adjacent, laths (white arrows in Figure 1C) for the formation of a calcite foil/sheet (white stars in Figure 1B), the association of very few, two to three, foils/sheets to a folium (colored dots in Figure 1C) and the strongly structured horizontal and vertical overlapping of folia in a foliated unit (Figure 1B,C) produce the graded arrangement of calcite c- and a*-axes in the foliated unit (Figure 2B) and the assembly of foliated units. The result, for a conglomerate of foliated units, is, in 3D space, a cone-shaped orientation distribution of calcite c- and a*-axes and, in 2D micrographs, a ring-shaped orientation distribution of calcite c-and a*-axes in the pole figures (Figures 7A–C and 9A). This is not only observed for *H. hyotis* but also for other gryphaeid and ostreid bivalve foliated units ([4] and Figures S3 and S4). The tilt of calcite c-axis by about 20° to 30°, relative to the inner shell surface normal, and to the growth direction of the shell toward the interior are observable from the pole figure (e.g., Figure 12A,B). This characteristic has also been reported for other Ostreidea shells [6,11]. The ring-shaped pattern of calcite crystallographic axes distributions is outstanding and has not yet been observed for the textures of other Ca-carbonate structural materials, neither biologically secreted nor man-made.

Figure 10 illustrates examples of the different texture patterns of calcitic microstructures secreted by marine organisms. Three of these (Figure 10A–C) show structural–crystallographic compatibility with the texture pattern of the *H. hyotis* foliated microstructure.

1. The *H. hyotis* conical and ring-shaped distribution of calcite c-axes orientation is not uniform but contains maxima (Figure 9A). For the measurement shown in Figure 6, we could distinguish 10 different c-axes maxima (Figure 10B,C). When these maxima are individually selected, an axial texture appears to be present for all these maxima (see pole figures in Figure 6C). Furthermore, Checa et al. [22] suggest a sheet or axial texture for the foliated shell microstructure of *Magallana angulata* (Lamarck, 1819). In Figures 10A and S5, we give an example of an axial texture of a biological calcite. The axial texture pattern [44,46] needs to have for, e.g., calcite, a clustered mode of calcite c-axes orientation with the corresponding three a*-axes orientations scattering on a great circle, thus, not forming any a*-axes clusters. This texture pattern is very common for biocarbonate hard tissues [46], e.g., it is the texture pattern of modern rhynchonellid brachiopod shells. In Figure 10A, we give an example of an axial texture for the shell of the modern brachiopod *Liothyrella neozelanica* (Thomson, 1918). Compare, in particular, the orientation distribution of the a*-axes for the foliated shell of *H. hyotis* with the orientation distribution of a*-axes for the shell of *L. neozelanica*. In the pole density distributions for *H. hyotis* we observe, for all three a*-axes, an individual and a substructured cluster (Figure 6C). This is not the case for the axial texture of brachiopod shell calcite (Figure 10A, and [45]).
2. In this study, we report the graded nature of calcite c- and a*-axes orientation for the foliated units. This characteristic is exceptional, as both crystallographic axes of the calcite have a graded orientation distribution. The gradedness for one of the crystallographic axes of biocalcite or bioaragonite has already been observed, e.g., in the case of terrestrial isopods (e.g., Huber et al. [49]). However, gradedness in all crystallographic axes of biocalcite or bioaragonite has, to the knowledge of the authors, been reported only twice so far, and the present study is the second study. The calcite of ommatidial lenses of the compound eyes of isopods has a graded c- and a*-axes orientation distribution [46]. The latter is well visible from the elongated appearance of the c- and the a*-axes orientation distributions in the pole figures (Figures 10B and S6). Nonetheless, even though they are graded in c- and a*-axes orientation, ommatidial lens with calcite c- and a*-axes do not form ring-shaped

orientation distributions but rather clear-cut individual maxima for the c- and the three a*-axes (see the pole figure in Figure 10B). The latter is also the case when the Euler angles are rotated in the virtual chamber (see pole figures in Figure S6). Thus, the texture of the ommatidial calcite lenses must be addressed as being single-crystal-like, with a graded orientational organization for all crystallographic axes of the calcite.

3. As shown in this contribution, the formation of conical and ring-shaped crystallographic axes orientation distributions is a hallmark of *H. hyotis* foliated calcite. Conical and ring-shaped c-axes orientation distributions are also observed for the microstructure of Mg calcite–hydrogel spherulites (Figures 10C, S7 and S8 and [47,48]). The conical and ring-shaped orientation distribution of spherulite c-axes is comparable to the c-axis texture pattern of *H. hyotis* foliated calcite; even more, we find, for both the spherulitic and the foliated c-axis ring, the development of orientation maxima within the stereographic projections of the c-axes rings (Figure 11A).
   Nevertheless, there are two main crystallographic differences between the foliated and the spherulitic texture:
   (i) For the spherulitic texture, we do not find formation of conical distributions for the a*-axes (see pole figures in Figures 10C, S7 and S8).
   (ii) Runnegar et al. [11], Checa et al. [6] and Checa et al. [22] report that the c-axis of the foliated crystals is tilted relative to the inner shell surface normal by 20° to 30° for the Ostreoidea species that were investigated in their studies. This is also what we deduce from the c-axis pole figures for the foliated layer of *H. hyotis* (Figures 10D and 11A). However, in contrast to the c-axis distribution pattern of the foliated texture, calcite c-axis poles of the spherulites, cover a significantly larger portion of the pole figure. In essence, even though we see some correspondences between the structural–crystallographic characteristics of the textures discussed above and the texture pattern of *H. hyotis* foliated calcite, none of these textures entirely reflect the texture pattern of the *H. hyotis* foliated calcite microstructure.

4. Thus, what is the structural model that addresses the foliated microstructure and texture in *H. hyotis*?
   It has often been described that the foliated microstructure of Ostreoidea shells consists of arrays of folia [4,6,11,12,30,54]. However, what is the correct term for the microstructure and corresponding texture of the Ca-carbonate shell section shown in Figure 11C? The *H. hyotis* foliated microstructure is, with our current insights, describable to some extent with a turbostratic-like arrangement of foliated units (Figure 11C). The formation of a turbostratic microstructure occurs, for example, by the settling of clay particles and groups of parallel arrays of clay platelets in clay–water suspension systems [42,43]. However, although the clay platelets are assembled in a cluster of platelets, more or less, in parallel, adjacent individual clay platelets in the cluster are rotated randomly, not structured, relative to each other. The clay clusters settle in a clay-water suspension system in a turbulent way, and, when settled, the clusters become variously misoriented relative to each other. This microstructure is a model that can be used to describe the microstructure of the *H. hyotis* foliated shell layer. The latter is formed of horizontally and vertically structured folia (Figure 1A–D), and the foliated shell layer comprises an assembly of variously sized and oriented foliated units (Figures 1D and 11B); the foliated shell has a very low MUD value (see the MUD values of 6 or 9 for the EBSD maps in Figures 5B and 9A), indicating a very low strength of foliated unit co-orientation in the shell. Accordingly, we can address the texture pattern of the *H. hyotis* microstructure as being turbostratic-like (see also [4]. For a further discussion of the foliated texture, see [30]).

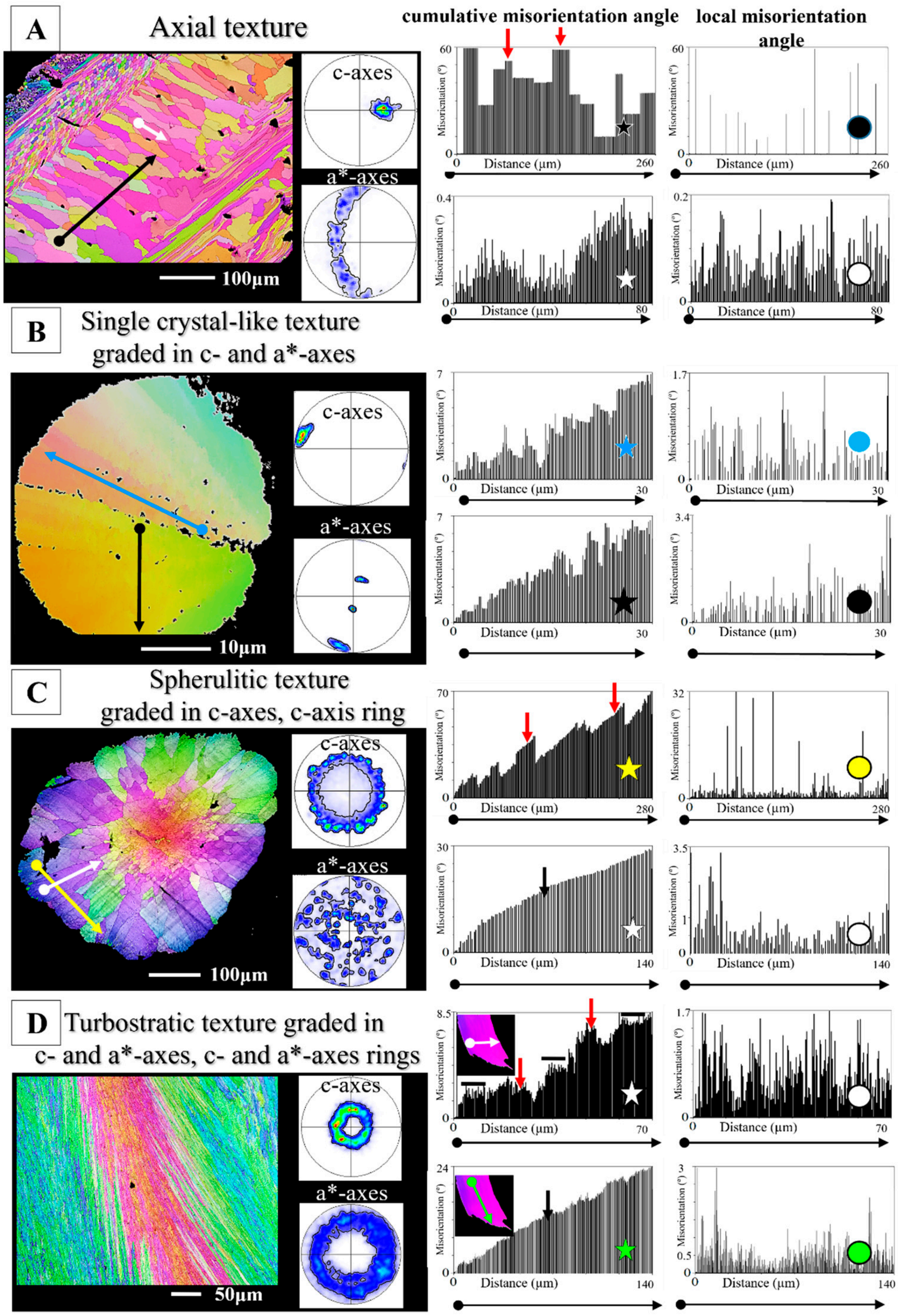

Figure 10. Structural and crystallographic characteristics of calcite–polymer composites with different microstructures, texture patterns and cumulative misorientations along trajectories a to b. Red and black arrows in the degree of misorientation-distance diagrams point to the difference in the course of the misorientation for a column of the brachiopod shell and a spherulitic crystal in the spherulite aggregate. The black, white, blue and yellow stars give in the misorientation angle-distance diagrams cumulative misorientation (misorientation relative to first point). The black, white, blue, yellow dots give in the misorientation angle-distance diagrams local misorientation (misorientation from point to point). The black, white, blue, yellow arrows in Figure 10A–D visualize the trace of the trajectory on the EBSD map and below the corresponding misorientation angle-distance diagram. (**A**): The three-layered shell of the modern calcitic brachiopod *Liothyrella neozelanica* (Thomson, 1918), (**B**): ommatidial calcite of the terrestrial isopod *Tylos europaeus* (Arcangeli, 1938), (**C**): calcite–agarose hydrogel composite aggregate, (**D**): *Hyotissa hyotis*.

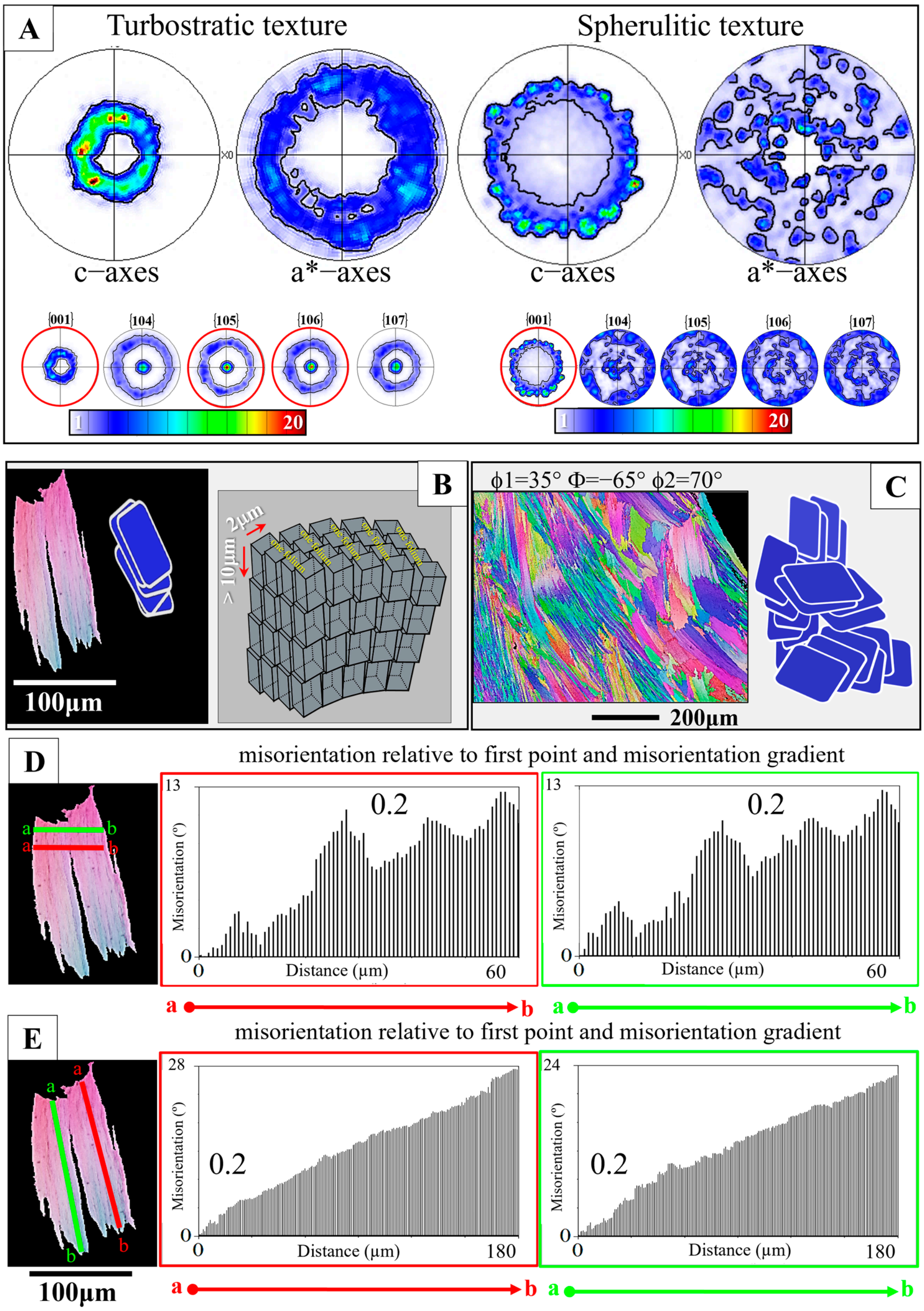

Figure 11. The juxtaposition of the turbostratic and the spherulitic texture patterns of calcite–polymer composites. (**A**): Left: the texture pattern of *Hyotissa hyotis* foliated calcite; right: the texture pattern of a calcite–agarose composite aggregate. (**B**): At left, a foliated unit of *H. hyotis* with a stack of sketched platelets, the latter indicating a possible assembly of folia in the foliated unit. (**B**): At right, sketch of a mesocrystal. A *mesocrystal* is a mesoscopically structured crystal, consisting of submicrometer-sized crystallites. These are organized within an individual mesocrystal with a crystallographic register [39–41]. In the sketch for a mesocrystal (right in (**B**)), we see rotated 'platelets', with each 'platelet' consisting of crystallites, arranged in the 'platelet' with strong co-alignment and somecrystallographic register. The sketched crystal, indicating a mesocrystal, has a hierarchical, crystallographically, highly regulated arrangement of its crystalline components, as is the case in a *H. hyotissa* foliated calcite unit (e.g., left in (**B**)). (**C**): EBSD measurement visualizing the arrangement of foliated units in the *H. hyotis* shell, in particular, visualizing the low degree of co-alignment of the foliated units. Right in (**C**): Sketch of a

turbostratic arrangement of platelet-comprising units. (**D**,**E**): Misorientation angle versus distance diagrams, along differently oriented trajectories a, b, visualizing the difference in smoothness of the course of cumulative misorientation for trajectories perpendicular to the long axis of the folia (**D**) and trajectories parallel to the long axis of the folia (**E**). The latter is a structural characteristic of a turbostratic texture.

4.1.2. The Cumulative and Local Misorientations

The misorientation angle diagrams reflect many microstructure and texture characteristics. In Figure 10, we show the course of the misorientation angle for cumulative (the colored stars in Figure 10) and local misorientation (the colored dots in Figure 10) along trajectories a to b for the different calcite microstructures and textures. For each hard tissue example, we give two transversal trajectories, and their direction and site are indicated in the corresponding EBSD maps. The following factors should be noted:

1. The difference in the course of the cumulative misorientation angle along the trajectories between the calcite microstructure that has an axial texture (Figure 10A) and the three other calcite microstructures and textures that display a different texture pattern (Figure 10B–D). In contrast to the calcite of the brachiopod shell, the ommatidial, composite aggregate and foliated calcite have some type of graded arrangement. Gradedness in crystal orientation is well visible from the course of the misorientation angle of the cumulative misorientation angle–distance diagrams, irrespective of the orientation of the trajectories (see the colored stars in Figure 10A–D).
2. However, even though the calcite crystals of the microstructures that are shown in Figure 10B–D have some graded arrangements, we find significant differences in the roughness of the course of the cumulative misorientation along the trajectory. This is the result of the different microstructure patterns and morphologies of crystal units, as is the case for ommatidial, spherulitic and foliated calcite.

The bulk of the brachiopod *L. neozelanica* shell consists of column-shaped prisms that are variously sized and, in general, strongly misoriented relative to each other; see the course of the corresponding cumulative misorientation diagram and note that misorientation between the prisms is several tens of degrees (the cumulative and local misorientation diagrams marked with a black star and dot in Figures 10A and S5). However, the calcite within a columnar prism is strongly co-oriented; the degree of both cumulative and local misorientation is below 0.5° (the cumulative and local misorientation diagrams marked with a white star and dot in Figure 10A). Calcite crystallites within a column/prism are arranged in parallel and are not misoriented to each other. This is the reason for the fact that we find in the cumulative misorientation diagram a plateau in the degree of misorientation for the individual columns/prisms (see red arrows in Figure 10A).

Due to the gradedness of calcite crystal assembly (Figure S6), ommatidial calcite shows, a fairly smoothly increasing misorientation angle with distance, for the cumulative misorientation and both trajectories, and a slightly increased misorientation between the crystal units of the microstructure (blue and black stars and dots in Figure 10B).

Due to the gradedness of calcite assembly in the calcite–agarose hydrogel spherulite, we find in the cumulative misorientation diagrams, along both trajectories, a smooth increase in misorientation angle and a low degree of misorientation between the crystal units comprising the spherulitic microstructure (yellow and white stars and dots in Figures 10C, S7 and S8). Nonetheless, note the two specific structural characteristics for the spherulite:

1. Increase in cumulative misorientation along a trajectory placed in an individual subunit of the spherulite (white arrow, indicating the trajectory and white star in the cumulative misorientation diagram) is exceptionally smooth (black arrow in Figure 10C). This indicates that the calcite crystal arrangement within a spherulitic unit is highly structured.

2. When the trajectory crosses adjacent spherulite sectors (yellow arrow for the trajectory, yellow stars in Figure 10C), the different spherulitic units are strongly misoriented to each other. We see from the course of cumulative misorientation that individual spherulitic units are also spherulites. For individual spherulitic units, we also observe a smooth increase in the course of the cumulative misorientation with distance (red arrows in Figure 10C).

For the also graded assembly of folia in a foliated unit, we find an increase in the misorientation angle with distance along the trajectory in the cumulative misorientation diagram (white and green stars in Figure 10D) and a slightly increased misorientation between folia in the local misorientation diagram. The degree of misorientation between folia resembles the degree of misorientation between the granular units of the ommatidial calcite. Nonetheless, for the foliated units that comprise the foliated shell of *H. hyotis*, we observe the following findings:

(i) When the trajectory runs parallel to the length of the foliated unit, the course of the cumulative misorientation is very smooth (black arrow in cumulative misorientation diagram in Figure 10D);
(ii) When the trajectory runs orthogonal to the length of the foliated unit, the course of the cumulative misorientation is uneven and jagged (red arrows in the cumulative misorientation diagram in Figure 10D).

This indicates that in one direction (the length of the unit), there is a very regulated structuring of the folia in a foliated unit, while in the other direction (perpendicular to the length of the unit), there is some regulation in the folia arrangement, but it is significantly less structured in comparison to the trajectory that runs parallel to the length of the unit (see also Figures 2 and 3). The misorientation gradient along the differently oriented trajectories for a foliated unit is the same (Figure 3). Thus, the degree of misorientation is similar and not dependent on the course of the trajectory. Nonetheless the degree of folia regularity differs for the different orientations of the trajectories taken on the foliated units.

The misorientation diagrams, in particular the cumulative misorientation diagrams, highlight the characteristics of the different microstructures and textures of the discussed Ca-carbonate hard tissues (Figure 10). We conclude from our EBSD data analysis that (i) the gradedness of both the crystallographic axes of the foliated calcite and (ii) the difference in the course of the cumulative misorientation angle with distance demonstrates that the microstructure and texture of the foliated shell layer of *H. hyotis* is neither spherulitic, noraxial nor single-crystal-like. Based on the structural and crystallographic knowledge that we have today for the foliated shell layer of *H. hyotis*, the foliated microstructure and texture of the latter can be addressed asturbostratic-like, having a turbostratic organization arrangement of the foliated units and subunits in the foliated microstructure (Figures 10 and 11).

4.1.3. The Coherence Between the Foliated and the Adjacent Shell Layers

As described and discussed above, the texture pattern of Ostreoidea foliated calcite is specific and outstanding (this study and Sancho Vaquer et al. [4]). Figures 7, 8, S3 and S4 highlight that, in addition to the ring-shaped distribution of calcite c- and a*-axes, we find strong clusters for the orientation of the {105} and {106} plane normals (Figures 7, 8, S3 and S4). The latter includes the foliated shell of *H. hyotis* and other Ostreoidea species (Figures 7, 8, S3 and S4). The corresponding planes are, more or less, parallel to the inner shell surface. When taking the entire shell into consideration and the orientation patterns of the crystallographic axes of crystals that form the adjacent shell layers (Figures 12 and 13), we observe the following:

1. The textures of myostracal aragonite and columnar prismatic calcite are axial. The c-axes orientation of pallial and adductor myostracal prisms is perpendicular to the inner shell surface (this study and Hoerl et al. [55]), as is also the case for the c-axis orientation of columnar calcite (this study and Sancho Vaquer et al. [4]).

2. The orientation directions of the {105} and{106} plane normals of the foliated calcite fall into the center of the c-axis rings in the stereographic projection (arrows in Figure 12A,B, black and blue arrow in Figure 13B top).
3. The c- axis direction of the axially textured myostracal aragonite and axially textured columnar calcite falls together with the joint orientation cluster of the {105} and {106} plane normals of the foliated calcite (red and blue arrows in Figure 12A,B, red and green arrows in Figure 13D,E).

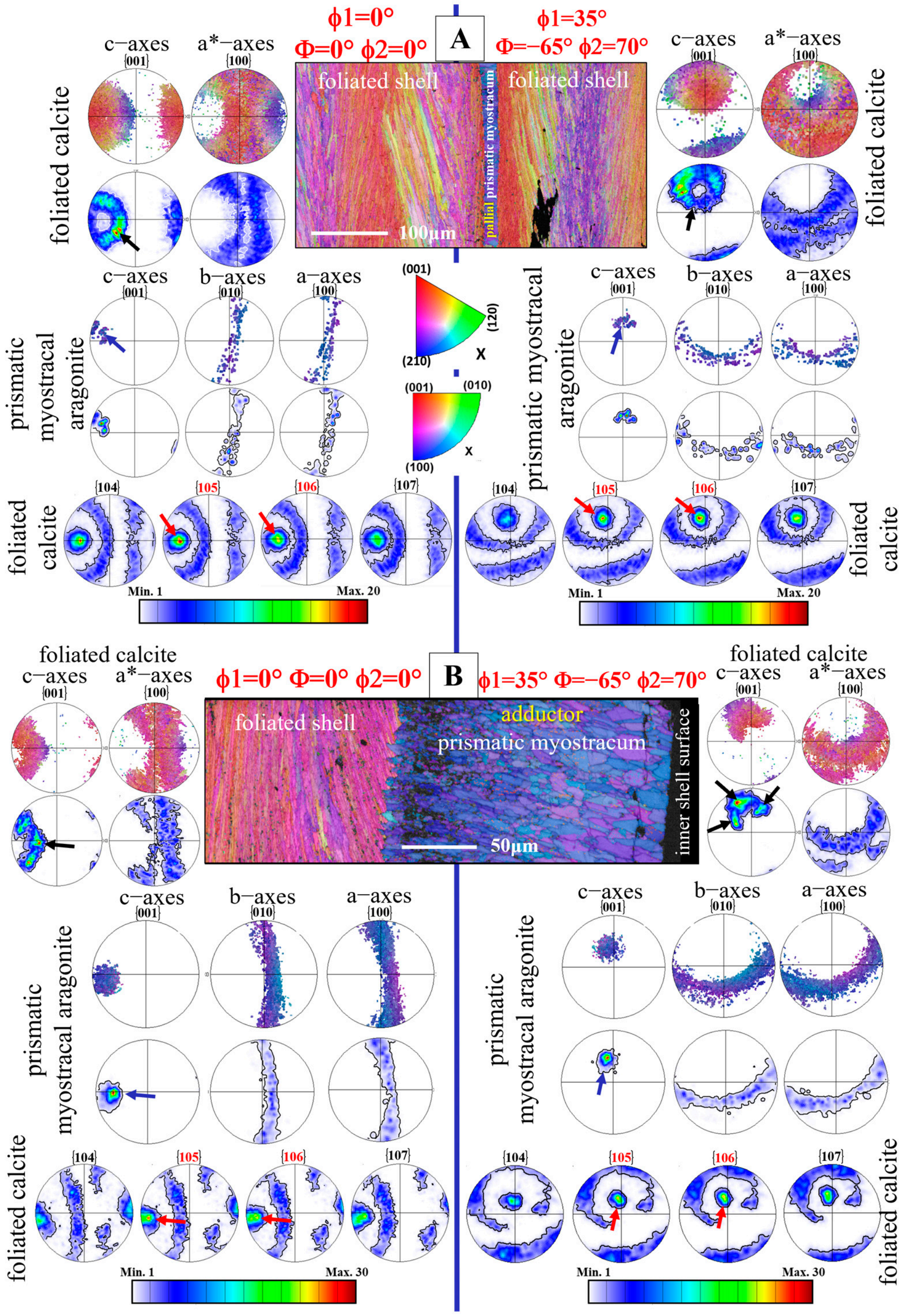

Figure 12. The alignment or/and misalignment of plane orientations of adjacent shell layers of *Hyotissa hyotis* shells. (**A**,**B**): The crossover from foliated calcite to myostracal aragonite. Black arrows point to the c-axes ring of the foliated calcite. Blue arrows point to the c-axis orientation of myostracal aragonite. Red arrows point to the {105} and {106} plane normal orientations.

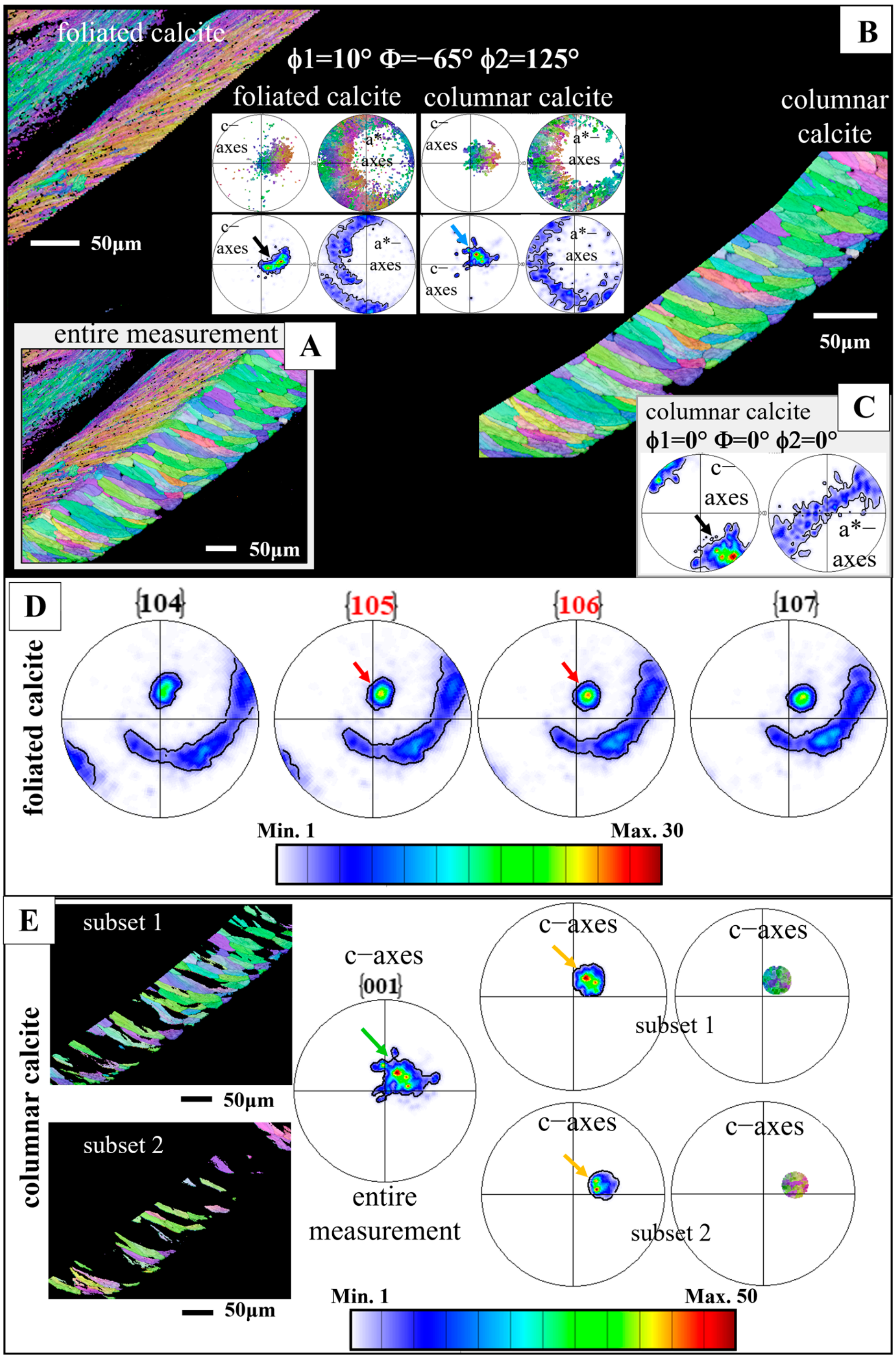

Figure 13. The alignment or/and misalignment of plane orientations of adjacent *Hyotissa hyotis* shell layers. (**A**,**B**): The crossover from foliated to columnar calcite. The black arrow in (**B**) points to formation of part of the c-axis orientation ring for the foliated shell portion. (**C**): The c- and a*-axes orientation of columnar calcite. The black arrow points to the c-axis cluster of the columnar shell portion. Note the difference in texture for the columnar (axial) and the foliated (turbostratic-like) shell. Accordingly, we find a c-axis cluster for the columnar shell and ring formation in c-axis orientation for the foliated shell. (**D**): Orientation of {105} to {107} plane normal for the calcite of the foliated shell. Red arrows point to the orientation of the {105} and {106} plane normals. (**E**): The c-axis orientation of columnar calcite and of the corresponding pole figures; the entire measurement is given in (**B**,**C**). Green arrow indicates the substructuring of the calcite c-axis cluster. Yellow arrows indicate the position of the two calcite subclusters in the pole figure.

Thus, the coherence of the columnar prismatic calcite, the foliated calcite and myostracal aragonite in the shell is given with the co-alignment of columnar prismatic calcite c-axes with the orientation of the {105}, {106} plane normals of the foliated calcite and the orientation of the myostracal aragonite c-axes.

5. Conclusions

The Ostreoidea are sessile marine organisms that live mainly in tidal to subtidal water depths and have adapted to a wide range of salinities. Although many are short-lived, they often secrete thick and fracture-resistant calcitic shells. The largest part of the shell by volume is formed of foliated calcite. The foliated shell layer has a hierarchical microstructure and is formed of laths, folia and foliated units. Assemblies of foliated units interdigitate in an intricate way and generate the foliated layers of the shell.

In this article, we characterize, from a crystallographic point of view, the nature of the foliated calcite texture of the gryphaeid oyster *Hyotissa hyotis*. Namely, the texture of individual folia, individual foliated units and assemblies of foliated units. We used low kV, high-resolution EBSD as the characterization technique and drew our conclusions for the structural nature of the foliated calcite and the association of crystallographic aspects derived from characteristics of the foliated microstructure and special features of the foliated texture.

We infer the following conclusions for the foliated texture of *H. hyotis*:

1. The calcite of a folium, consisting of two to four sheets of vertically overlapping lath-shaped crystals, is very co-oriented; it is almost single-crystalline. Accordingly, the texture pattern of a folium is single-crystal-like (Figure 4A).
2. Adjacent folia are misoriented relative to each other by less than 1°; accordingly, the calcite of few (<10) adjacent folia is also very co-oriented and the texture of a stack of folia is also single-crystal-like (Figure 4D).
3. Individual foliated units, comprising a multitude of folia, show a graded pattern of calcite c- and a*-axes orientation distribution. This results from the strongly structured and staggered vertical and lateral arrangement of the folia in a foliated unit. The texture of an entity of a few foliated units shows some comparable features to an axial texture (Figure 6C); however, the individual c- and a*-axes clusters are substructured by subunits and misoriented to each other by 10° to 20° (pole figure 1 in Figure 5E, insert in EBSD map of c-axis cluster 1 in Figure 6C).
4. The gradedness of c- and a*-axes orientation in a foliated unit affects assemblies of foliated units, where calcite c- and a*-axes orientations form, in 3D, conical, and in 2D pole figures, ring-shaped, distributions (Figure 9A). This is a crystallographic characteristic that is, so far, observed only in the foliated calcite of Ostreoidea shells (this study and [4]). Accordingly, the texture pattern of assemblies of foliated units is neither single-crystalline nor axial.
5. We find very high crystal co-orientation strengths (MUD > 600) for the laths in folia and the folia in a foliated unit. However, there are very low crystal co-orientation strengths (MUD < 10) for the conglomerates of foliated units forming the foliated shell. The latter is a very characteristic feature of the foliated shell layer of Ostreoidea shells.
6. The course of misorientation between folia along trajectories is (i) very smooth when the trajectory runs along the length of a foliated unit; however, (ii) it is rough when the trajectory runs normal to the long axis of a folium. This is specific to Ostreoidea shell foliated units. Hence, along the length of a foliated unit, the arrangement of foils is highly structured, while perpendicular to the length of a foliated unit; thus, the arrangement from folium to folium is less regular.

7. The crystals that form the foliated shell of *H. hyotis* are lath-shaped units with arrowhead endings. Arrowhead development is present only on one of the two ends of a lath. The arrowhead tip points towards the growth direction of the shell and is generated by plains that are, more or less, parallel to the inner shell surface.
   In the pole figures we find that the {105} or/and {106} plane normals form a strong cluster in the relevant pole figures; their orientation direction is parallel to the orientation direction of myostracal aragonite and of columnar calcite c-axes, the shell layers that are adjacent to the foliated layer of the shell.
8. The c-axes pole figures show that foliated calcite c-axes are oriented at an angle of 20° to 30° to the orientation of the inner shell surface normal, a characteristic also reported by Runnegar [11] and Checa et al. [6] for other Ostreoidea species.
9. We discuss potential texture patterns for the foliated shell layer of *H. hyotis*, such as axial, spherulitic and single-crystal-like patterns, with graded calcite c- and a*-axes orientations, as well as turbostratic-like texture patterns.
10. Taking all the crystallographic and structural characteristics that we obtained from our EBSD measurements and, in particular, from EBSD data evaluation, we conclude that, at present, a turbostratic-like texture model fits, at least to some degree, the texture pattern of the assemblies of *H. hyotis* foliated units.

Supplementary Materials: The following supporting information can be downloaded at https://www.mdpi.com/article/10.3390/cryst15030244/s1, Figure S1: Illustration of the crystallographic terms defined in the terminology section; Figure S2: Misorientation angle versus distance diagrams and misorientation gradients (the number in the misorientation angle–distance diagrams) (C to F) for individual foliated units present in *Hyotissa hyotis* shells (A). A: The selected crystals are shown in color in the EBSD band contrast map; the colors code for crystal orientation. B: Pole figures for each selected crystal. Well visible in the map and in the pole figures is the gradedness in c- and a*-axes orientation. Misorientation between crystals is shown along trajectories a to b, c to d, e to f; the cumulative misorientation is shown, misorientation relative to the first point on the trajectory (C to F). For each chosen foliated unit, trajectories run parallel as well as orthogonal to the length of the foliated unit. We observe for all trajectories a smooth increase in misorientation angle, relative to the first point on the trajectory; this characteristic is particularly well developed for trajectories that are parallel to the length of a folium (trajectories are shown in green). The numbers within the misorientation angle-distance diagrams give the misorientation gradient for the corresponding diagram. We find very low and, for the chosen foliated units (this Figure and Figure 3) very comparable misorientation gradients; Figure S3: The orientation of various calcite planes and calcite c- and a*-axes for the foliated shell of other gryphaeid oysters, e.g., *Hyotissa mcgintyi* (H. W. Harry, 1985) and *Neopycnodonte cochlear* (Poli, 1795). We see strong orientation maxima in the {001}, {105}, {106} and {107} pole figures; Figure S4: The orientation of various calcite planes and calcite c- and a*-axes for the foliated shell of the ostreid oysters *Magallana gigas* (Thunberg, 1793), *Ostrea stentina* (Payraudeau, 1826) and *Ostrea edulis* (Linnaeus, 1758). We see strong orientation maxima in the {001}, {105}, {106} and {107} pole figures; Figure S5: Microstructure, axial texture and misorientation angle–distance diagrams for the calcitic shell of the modern brachiopod *Liothyrella neozelanica* (Thomson, 1819). Well observable is the axial texture of the calcite; see pole figures in (A) and (B). An axial texture is given when we observe clustering in c-axes orientation with a scattering in corresponding a*-axes orientations on a great circle that is perpendicular to the texture axis direction. C: Misorientation angle-distance diagrams, misorientation relative to the first point) for trajectories A to B (on the fibrous shell portion) and C to D (on the columnar shell portion). Note the difference in cumulative misorientation between brachiopod calcite and the foliated calcite of *H. hyotis* units. The texture pattern of brachiopod calcite is different to the texture pattern of *H. hyotis* foliated calcite. Accordingly, we find a strong difference in cumulative misorientation between the calcite of the brachiopod shell and the calcite of the foliated *H. hyotis* shell. Contrasting to the foliated shell of *H. hyotis*, for the brachiopod shell we find a wide range in misorientation between the shell-forming crystals, and do not observe any gradedness in c- and a*-axes orientation; Figure S6: Omatidial calcite of the terrestrial isopod *Tylos europaeus*. The calcite has a granular microstructure (see the gray-colored EBSD band contrast measurement images). Calcite arrangement is graded (see in the EBSD maps the gradual change in color). The latter is also well observable in the pole figures. However, despite c- and a*-axes gradedness, we do not observe in the pole figures a ring-shaped c- and a*-axes orientation distribution; Figure S7: Microstructure, spherulitic texture (A) and misorientation angle-distance diagrams for trajectories a to b (B to E) taken on a calcite-hydrogel spherulite. The spherulite consists of small subunits; Figure S8: Microstructure, spherulitic texture (A) and misorientation angle-distance diagrams for trajectories a to b (B to E) taken on a calcite-hydrogel spherulite. Large spherulitic subunits seam the outer portion and rim of the spherulite, an assembly of small spherulitic crystallites forms the central portion of the spherulite.

Author Contributions: E.G. wrote the manuscript and made the EBSD measurements, A.S.V. evaluated the EBSD data and helped write the manuscript, A.G.C. discussed EBSD data and helped write the manuscript, W.W.S. discussed EBSD data and helped with the crystallographic interpretation of crystal orientations, C.S. and E.M.H. helped write the manuscript. All authors have read and agreed to the published version of the manuscript.

Funding: W.W.S., E.G. and A.S.V. are funded by the German Research Council Programmes GR 9/1234, SCHM 930/11-2. A.G.C. and C.S.C are funded by projects PID2023-146394NB-I00 and PID2020116660GB-I00 (Spanish Ministry of Science and Innovation: MCIN/AEI/10.13039/501100011033/).

Data Availability Statement: The raw data supporting the conclusions of this article will be made available by the authors upon request.

Acknowledgments: We thank Sebastian Hoerl for evaluating many EBSD data sets, including AZTec Crystal, for his help with the interpretation of crystal orientation data and for his many, in general, very useful comments on the manuscript. We thank Lisa Kreitmeier for the preparation of some Ostreoidea samples. A.G.C. acknowledges the Unidad Científica de Excelencia UCE-PP2016-05 (University of Granada) and the Research Group RNM363 (Junta de Andalucía).

Conflicts of Interest: The authors declare no conflicts of interest.

References

1. Brand, U.; Veizer, J. Chemical Diagenesis of a Multicomponent Carbonate System; 1, Trace Elements. *J. Sediment. Res.* **1980**, *50*, 1219–1236. [CrossRef]
2. Carriker, M.R.; Palmer, R.E.; Sick, L.V.; Johnson, C.C. Interaction of Mineral Elements in Sea Water and Shell of Oysters (*Crassostrea virginica* (Gmelin)) Cultured in Controlled and Natural Systems. *J. Exp. Mar. Biol. Ecol.* **1980**, *46*, 279–296. [CrossRef]
3. Carriker, M.R.; Palmer, R.E.; Prezant, R. Functional Ultramorphology of the Dissoconch Valves of the Oyster *Crassostrea virginica*. *J. Shellfish Res.* **1981**, *70*, 139–183.
4. Sancho Vaquer, A.; Griesshaber, E.; Salas, C.; Harper, E.M.; Checa, A.G.; Schmahl, W.W. The Diversity of Crystals, Microstructures and Texture That Form Ostreoidea Shells. *Crystals* **2025**. submitted.
5. Checa, A.G. Physical and Biological Determinants of the Fabrication of Molluscan Shell Microstructures. *Front. Mar. Sci.* **2018**, *5*, 353. [CrossRef]
6. Checa, A.G.; Esteban-Delgado, F.J.; Rodríguez-Navarro, A.B. Crystallographic Structure of the Foliated Calcite of Bivalves. *J. Struct. Biol.* **2007**, *157*, 393–402. [CrossRef] [PubMed]
7. Dungan, C.F. Aragonite-Fiber Calcification of the Hinge Ligament Mechanical Antagonist to Valve Adduction in Oysters. *J. Shellfish Res.* **2008**, *27*, 1004–1005.
8. Lemer, S.; González, V.L.; Bieler, R.; Giribet, G. Cementing Mussels to Oysters in the Pteriomorphian Tree: A Phylogenomic Approach. *Proc. R. Soc. B Biol. Sci.* **2016**, *283*, 20160857. [CrossRef]
9. Meng, Y.; Fitzer, S.C.; Chung, P.; Li, C.; Thiyagarajan, V.; Cusack, M. Crystallographic Interdigitation in Oyster Shell Folia Enhances Material Strength. *Cryst. Growth Des.* **2018**, *18*, 3753–3761. [CrossRef]
10. Mouchi, V.; Lartaud, F.; Guichard, N.; Immel, F.; de Rafélis, M.; Broussard, C.; Crowley, Q.G.; Marin, F. Chalky versus Foliated: A Discriminant Immunogold Labelling of Shell Microstructures in the Edible Oyster *Crassostrea gigas*. *Mar. Biol.* **2016**, *163*, 256. [CrossRef]

11. Runnegar, B. Crystallography of the Foliated Calcite Shell Layers of Bivalve Molluscs. *Alcheringa Australas. J. Palaeontol.* **1984**, *8*, 273–290. [CrossRef]
12. Taylor, J.D.; Kennedy, W.J.; Hall, A. The Shell Structure and Mineralogy of the Bivalvia Introduction. Nuculacea—Trigonacea. In *Bulletin of the British Museum (Natural History). Zoology Supplement*; British Museum: London, UK, 1969; Supplement 3; pp. 1–125. [CrossRef]
13. Checa, A.G.; Esteban-Delgado, F.J.; Ramírez-Rico, J.; Rodríguez-Navarro, A.B. Crystallographic Reorganization of the Calcitic Prismatic Layer of Oysters. *J. Struct. Biol.* **2009**, *167*, 261–270. [CrossRef] [PubMed]
14. Esteban-Delgado, F.J.; Harper, E.M.; Checa, A.G.; Rodríguez-Navarro, A.B. Origin and Expansion of Foliated Microstructure in Pteriomorph Bivalves. *Biol. Bull.* **2008**, *214*, 153–165. [CrossRef]
15. Okumura, T.; Suzuki, M.; Nagasawa, H.; Kogure, T. Characteristics of Biogenic Calcite in the Prismatic Layer of a Pearl Oyster, *Pinctada fucata*. *Micron* **2010**, *41*, 821–826. [CrossRef] [PubMed]
16. Yonge, C.M. *Oysters*; Collins: New York, NY, USA, 1960.
17. Harper, E.M. Post-Larval Cementation in the Ostreidae and Its Implications for Other Cementing Bivalvia. *J. Molluscan Stud.* **1992**, *58*, 37–47. [CrossRef]
18. Harper, E.M. Attachment of Mature Oysters (*Saccostrea cucullata*) to Natural Substrata. *Mar. Biol.* **1997**, *127*, 449–453. [CrossRef]
19. MacDonald, J.; Freer, A.; Cusack, M. Attachment of Oysters to Natural Substrata by Biologically Induced Marine Carbonate Cement. *Mar. Biol.* **2010**, *157*, 2087–2095. [CrossRef]
20. Banker, R.M.W.; Sumner, D.Y. Structure and Distribution of Chalky Deposits in the Pacific Oyster Using X-Ray Computed Tomography (CT). *Sci. Rep.* **2020**, *10*, 12118. [CrossRef]
21. Banker, R.; Vermeij, G.J. Oyster Microbial Communities and Implications for Chalky Deposit Formation. *Hydrobiologia* **2018**, *816*, 121–135. [CrossRef]
22. Checa, A.G.; Harper, E.M.; González-Segura, A. Structure and Crystallography of Foliated and Chalk Shell Microstructures of the Oyster *Magallana*: The Same Materials Grown under Different Conditions. *Sci. Rep.* **2018**, *8*, 7507. [CrossRef]
23. Galtsoff, P.S. The American Oyster, *Crassostrea virginica* (Gmelin). *Chesap. Sci.* **1965**, *6*, 199. [CrossRef]
24. Korringa, P. On the Nature and Function of "Chalky" Deposits in the Shell of Ostrea edulis Linnaeus. In *California Academy of Sciences*; 4th series; Creative Media Partners, LLC: Sacramento, CA, USA, 1951; Volume 27, pp. 133–158.
25. Checa, A.G.; Linares, F.; Maldonado-Valderrama, J.; Harper, E.M. Foamy Oysters: Vesicular Microstructure Production in the Gryphaeidae via Emulsification. *J. R. Soc. Interface* **2020**, *17*, 20200505. [CrossRef]
26. de Winter, N.J.; Vellekoop, J.; Vorsselmans, R.; Golreihan, A.; Soete, J.; Petersen, S.V.; Meyer, K.W.; Casadio, S.; Speijer, R.P.; Claeys, P. An Assessment of Latest Cretaceous *Pycnodonte vesicularis* (Lamarck, 1806) Shells as Records for Palaeoseasonality: A Multi-Proxy Investigation. *Clim. Past* **2018**, *14*, 725–749. [CrossRef]
27. Titschack, J.; Zuschin, M.; Spötl, C.; Baal, C. The Giant Oyster Hyotissa Hyotis from the Northern Red Sea as a Decadal-Scale Archive for Seasonal Environmental Fluctuations in Coral Reef Habitats. *Coral Reefs* **2010**, *29*, 1061–1075. [CrossRef]
28. Chateigner, D.; Hedegaard, C.; Wenk, H.-R. Mollusc Shell Microstructures and Crystallographic Textures. *J. Struct. Geol.* **2000**, *22*, 1723–1735. [CrossRef]
29. Hedegaard, C.; Wenk, H.-R. Microstructure and Texture Patterns of Mollusc Shells. *J. Molluscan Stud.* **1998**, *64*, 133–136. [CrossRef]
30. Schmahl, W.W.; Sancho Vaquer, A.; Checa, A.; Griesshaber, E. *The Very Specific Texture Motif of the Oyster Shell Turbostratic Foliated Microstructure*; Ludwig-Maximilians-Universität München: Munich, Germany, 2025.
31. Bieler, R.; Mikkelsen, P.M.; Lee, T.; Foighil, D.Ó. Discovery of the Indo-Pacific Oyster *Hyotissa hyotis* (Linnaeus, 1758) in the Florida Keys (Bivalvia: Gryphaeidae). *Molluscan Res.* **2004**, *24*, 149–159. [CrossRef]
32. Duprat-Bertazzi, G.; García-Domínguez, F. Reproductive Cycle of the Rock Oyster *Hyotissa hyotis* (Linné, 1758) (Griphaeidae) at the La Ballena Island, Gulf of California, México. *J. Shellfish Res.* **2005**, *24*, 987–993. [CrossRef]
33. Carriker, M.R.; Gaffney, P.M. A Catalogue of Selected Species of Living Oysters (Ostreacea) of the World. In *The Eastern Oyster: Crassostrea Virginica*; Kennedy, V.S., Newell, R.I.E., Eble, A.F., Eds.; Maryland Sea Grant: College Park, MD, USA, 1996; pp. 1–8.
34. Lindner, G. *Moluscos y Caracoles de Los Mares Del Mundo*; Omega: Barcelona, Spain, 1983.
35. Sevilla, M.L. *Las Ostras de México*; Limusa: Mexico City, Mexico, 1993.
36. Harry, H.W. Synopsis of the Supraspecific Classification of Living Oysters (Bivalvia: Gryphaeidae and Ostreidae). *Veliger* **1985**, *28*.
37. Abbott, R.T. *American Seachells*; Van Nostrand Reinhold Company: New York, NY, USA, 1974.
38. Hull, D.; Bacon, D.J. *Introduction to Dislocations*, 5th ed.; Butterworth-Heinemann: Oxford, UK, 2011; ISBN 978-0-08-096672-4.
39. Seto, J.; Ma, Y.; Davis, S.A.; Meldrum, F.; Gourrier, A.; Kim, Y.Y.; Schilde, U.; Sztucki, M.; Burghammer, M.; Maltsev, S.; et al. Structure-Property Relationships of a Biological Mesocrystal in the Adult Sea Urchin Spine. *Proc. Natl. Acad. Sci. USA* **2012**, *109*, 3699–3704. [CrossRef]
40. Ma, M.-G.; Cölfen, H. Mesocrystals—Applications and Potential. *Curr. Opin. Colloid. Interface Sci.* **2014**, *19*, 56–65. [CrossRef]
41. Bergström, L.; Sturm (née Rosseeva), E.V.; Salazar-Alvarez, G.; Cölfen, H. Mesocrystals in Biominerals and Colloidal Arrays. *Acc. Chem. Res.* **2015**, *48*, 1391–1402. [CrossRef] [PubMed]

42. Aylmore, L.a.G.; Quirk, J.P. Swelling of Clay–Water Systems. *Nature* **1959**, *183*, 1752–1753. [CrossRef]
43. Lutterotti, L. Total Pattern Fitting for the Combined Size–Strain–Stress–Texture Determination in Thin Film Diffraction. *Nucl. Instrum. Methods Phys. Res. Sect. B Beam Interact. Mater. At.* **2010**, *268*, 334–340. [CrossRef]
44. Schwartz, A.J.; Kumar, M.; Adams, B.L. (Eds.) *Electron Backscatter Diffraction in Materials Science*; Springer US: Boston, MA, USA, 2000; ISBN 978-1-4757-3207-8.
45. Simonet Roda, M.; Griesshaber, E.; Angiolini, L.; Rollion-Bard, C.; Harper, E.M.; Bitner, M.A.; Milner Garcia, S.; Ye, F.; Henkel, D.; Häussermann, V.; et al. The Architecture of Recent Brachiopod Shells: Diversity of Biocrystal and Biopolymer Assemblages in Rhynchonellide, Terebratulide, Thecideide and Craniide Shells. *Mar. Biol.* **2021**, *169*, 4. [CrossRef]
46. Griesshaber, E.; Yin, X.; Ziegler, A.; Kelm, K.; Checa, A.; Eisenhauer, A.; Schmahl, W.W. Patterns of Mineral Organization in Carbonate Biological Hard Materials. In *Highlights in Applied Mineralogy*; Heuss-Aßbichler, S., Amthauer, G., John, M., Eds.; De Gruyter: Berlin, Germany; Boston, MA, USA, 2017; pp. 245–272; ISBN 978-3-11-049734-2.
47. Yin, X.; Griesshaber, E.; Fernández-Díaz, L.; Ziegler, A.; García-García, F.J.; Schmahl, W.W. Influence of Gelatin–Agarose Composites and Mg on Hydrogel-Carbonate Aggregate Formation and Architecture. *Cryst. Growth Des.* **2019**, *19*, 5696–5715. [CrossRef]
48. Yin, X.; Weitzel, F.; Jiménez-López, C.; Griesshaber, E.; Fernández-Díaz, L.; Rodríguez-Navarro, A.; Ziegler, A.; Schmahl, W.W. Directing Effect of Bacterial Extracellular Polymeric Substances (EPS) on Calcite Organization and EPS–Carbonate Composite Aggregate Formation. *Cryst. Growth Des.* **2020**, *20*, 1467–1484. [CrossRef]
49. Huber, J.; Griesshaber, E.; Nindiyasari, F.; Schmahl, W.W.; Ziegler, A. Functionalization of Biomineral Reinforcement in Crustacean Cuticle: Calcite Orientation in the Partes Incisivae of the Mandibles of *Porcellio scaber* and the Supralittoral Species *Tylos europaeus* (Oniscidea, Isopoda). *J. Struct. Biol.* **2015**, *190*, 173–191. [CrossRef]
50. Yin, X.; Castro-Claros, J.D.; Griesshaber, E.; Salas, C.; Sancho Vaquer, A.; Checa, A.G.; Schmahl, W.W. Molluscs Generate Preferred Crystallographic Orientation of Biominerals by Organic Templates, the Texture and Microstructure of Caudofoveata (Aplacophora) Shells. *Sci. Rep.* **2024**, *14*, 13469. [CrossRef]
51. Castro-Claros, J.D.; Yin, X.; Salas, C.; Griesshaber, E.; Hörl, S.; Checa, A.G.; Schmahl, W.W. Biomineral Crystallographic Preferred Orientation in Solenogastres Molluscs (Aplacophora) Is Controlled by Organic Templating. *Sci. Rep.* **2024**, *14*, 10309. [CrossRef]
52. Yin, X.; Castro-Claros, J.D.; Griesshaber, E.; Salas, C.; Checa, A.G.; Schmahl, W.W. Biological Control of Microstructure and Texture: Adapting Crystal Orientation to Biomaterial Function, as Observed for Polyplacophora Spicule Aragonite. *Mar. Biol.* **2025**. submitted.
53. Casella, L.A.; He, S.; Griesshaber, E.; Fernández-Díaz, L.; Greiner, M.; Harper, E.M.; Jackson, D.J.; Ziegler, A.; Mavromatis, V.; Dietzel, M.; et al. Hydrothermal Alteration of Aragonitic Biocarbonates: Assessment of Micro- and Nanostructural Dissolution–Reprecipitation and Constraints of Diagenetic Overprint from Quantitative Statistical Grain-Area Analysis. *Biogeosciences* **2018**, *15*, 7451–7484. [CrossRef]
54. Checa, A.G.; Yáñez-Ávila, M.E.; González-Segura, A.; Varela-Feria, F.; Griesshaber, E.; Schmahl, W.W. Bending and Branching of Calcite Laths in the Foliated Microstructure of Pectinoidean Bivalves Occurs at Coherent Crystal Lattice Orientation. *J. Struct. Biol.* **2019**, *205*, 7–17. [CrossRef] [PubMed]
55. Hoerl, S.; Griesshaber, E.; Häussermann, V.; Achterhold, C.; Amini, S.; Schmahl, W.W. *Calcite Crystal Organization and Architecture of the Muscle Scars, the Myotests of Modern Brachiopod Shells*; Ludwig-Maximilians-Universität München: Munich, Germany, 2025.